Article

Current Biology

Comprehensive Identification and Spatial Mapping of Habenular Neuronal Types Using Single-Cell RNA-Seq

Graphical Abstract

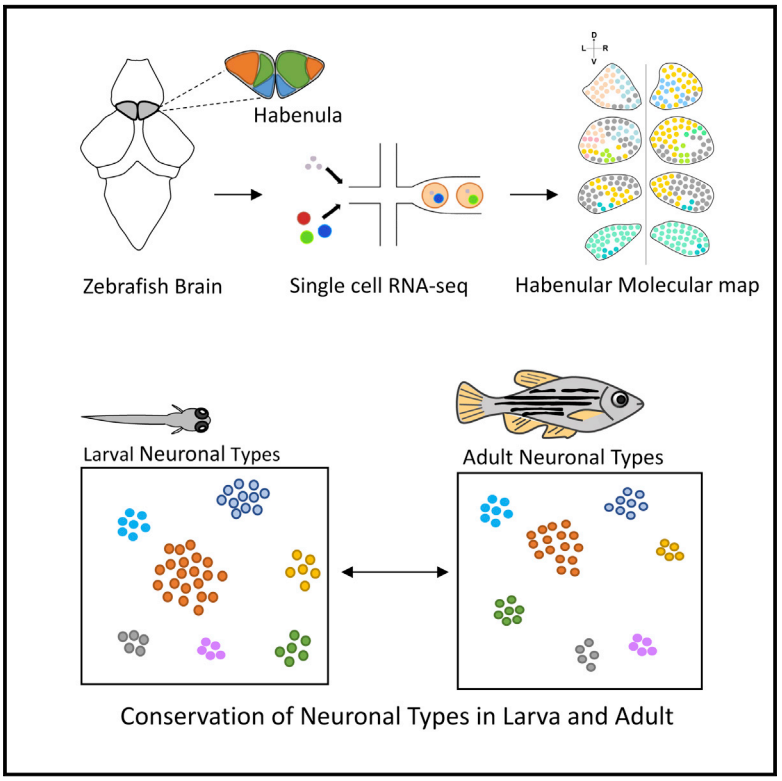

Highlights

- Establishment of a single-cell RNA-seq protocol for neurons in zebrafish
- Identification of 18 distinct habenular types
- Retention of neuronal types between larva and adult
- RNA-FISH and image registration to build a gene expression atlas

Authors

Shristi Pandey, Karthik Shekhar, Aviv Regev, Alexander F. Schier

Correspondence

p.shristi@gmail.com (S.P.), schier@fas.harvard.edu (A.F.S.)

In Brief

Pandey et al. use scRNA-seq to define more than a dozen different neuronal types in the zebrafish habenula. Cell types are retained between larva and adult.

Pandey et al., 2018, Current Biology *28*, 1052–1065
April 2, 2018
https://doi.org/10.1016/j.cub.2018.02.040

CellPress

CellPress

Current Biology
Article

Comprehensive Identification and Spatial Mapping of Habenular Neuronal Types Using Single-Cell RNA-Seq

Shristi Pandey,[1,*] Karthik Shekhar,[2] Aviv Regev,[2,3] and Alexander F. Schier[1,2,4,5,6,7,*]
[1]Department of Molecular and Cellular Biology, Harvard University, Cambridge, MA 02138, USA
[2]Klarman Cell Observatory, Broad Institute of MIT and Harvard, 7 Cambridge Center, Cambridge, MA 02142, USA
[3]Howard Hughes Medical Institute and Koch Institute of Integrative Cancer Research Department of Biology, Massachusetts Institute of Technology, Cambridge, MA 02140, USA
[4]Center for Brain Science, Harvard University, 52 Oxford Street, Cambridge, MA 02138, USA
[5]Biozentrum, University of Basel, Basel, Switzerland
[6]Allen Discovery Center for Cell Lineage Tracing, University of Washington, Seattle, WA 98195, USA
[7]Lead Contact
*Correspondence: p.shristi@gmail.com (S.P.), schier@fas.harvard.edu (A.F.S.)
https://doi.org/10.1016/j.cub.2018.02.040

SUMMARY

The identification of cell types and marker genes is critical for dissecting neural development and function, but the size and complexity of the brain has hindered the comprehensive discovery of cell types. We combined single-cell RNA-seq (scRNA-seq) with anatomical brain registration to create a comprehensive map of the zebrafish habenula, a conserved forebrain hub involved in pain processing and learning. Single-cell transcriptomes of ~13,000 habenular cells with 4× cellular coverage identified 18 neuronal types and dozens of marker genes. Registration of marker genes onto a reference atlas created a resource for anatomical and functional studies and enabled the mapping of active neurons onto neuronal types following aversive stimuli. Strikingly, despite brain growth and functional maturation, cell types were retained between the larval and adult habenula. This study provides a gene expression atlas to dissect habenular development and function and offers a general framework for the comprehensive characterization of other brain regions.

INTRODUCTION

The study of formation and function of neural circuits relies on the ability to identify specific cell types that are defined by location, morphology, connectivity, and molecular composition. Classical histological and gene expression analyses have recently been extended to single-cell technologies that enable *de novo* identification of cell types based on their transcriptomes [1–7]. Such studies have provided valuable resources for cataloging cell types but are limited in their comprehensive classification by the large number and diversity of neurons in vertebrate brains. This complexity results in low sampling of rare cell types even with recent technologies that allow profiling of thousands of individual neurons in a single experiment [8, 9]. With the possible exception of a single class of interneurons in the mouse retina, we lack comprehensive catalogs of cell types in any region of the vertebrate brain [10].

One scenario in which sampling limits can be overcome is in the case of specific and conserved brain regions in animals with compact size. To test this approach, we analyzed the zebrafish habenula, a small forebrain region that is composed of approximately ~1,500 neurons at the larval stage. The habenula is a conserved structure that plays fundamental roles in vertebrate neurophysiology and behavior [11]. It receives input from a large number of brain regions and can influence a wide range of behaviors, including sleep, pain processing, reward learning, and fear [11–13]. Its pathophysiology has been implicated in neurological disorders such as depression, schizophrenia, and addiction [14].

Current anatomical and molecular analysis partitions the zebrafish habenula into three major sub-regions: the *nptx2a*-expressing dorsolateral domain, the *gpr151/pou4f1*-expressing dorsomedial domain, and the *aoc1*-expressing ventral domain (Figure 1A). Neurons in these domains project to distinct downstream regions in the interpeduncular nucleus (IPN) and raphe nucleus, thus mediating distinct behavioral outputs [11, 15]. These domains are also homologous to distinct domains in the mouse habenula [16]. For instance, the ventral habenula of zebrafish shares gene expression and projection patterns with the mammalian lateral habenula [17]. Furthermore, domain-specific genes are often used as genetic handles in functional studies [18–20].

It has been unclear, however, whether individual neurons in these sub-nuclei represent a single neuronal type or a mixture of multiple types. In addition, the zebrafish habenula displays a remarkable left-right (L-R) asymmetry in gene expression and functionality [21]. A number of genes such as *adcyap1a*, *nrp1a*, *tac1*, *tac3a*, and *slc5a7a* are left-right asymmetric in the dorsal habenula [17, 22–25]. Recent studies have also shown left-right asymmetry in functional responses to light and odor in the left and right habenula, respectively [26–28]. It is also unclear

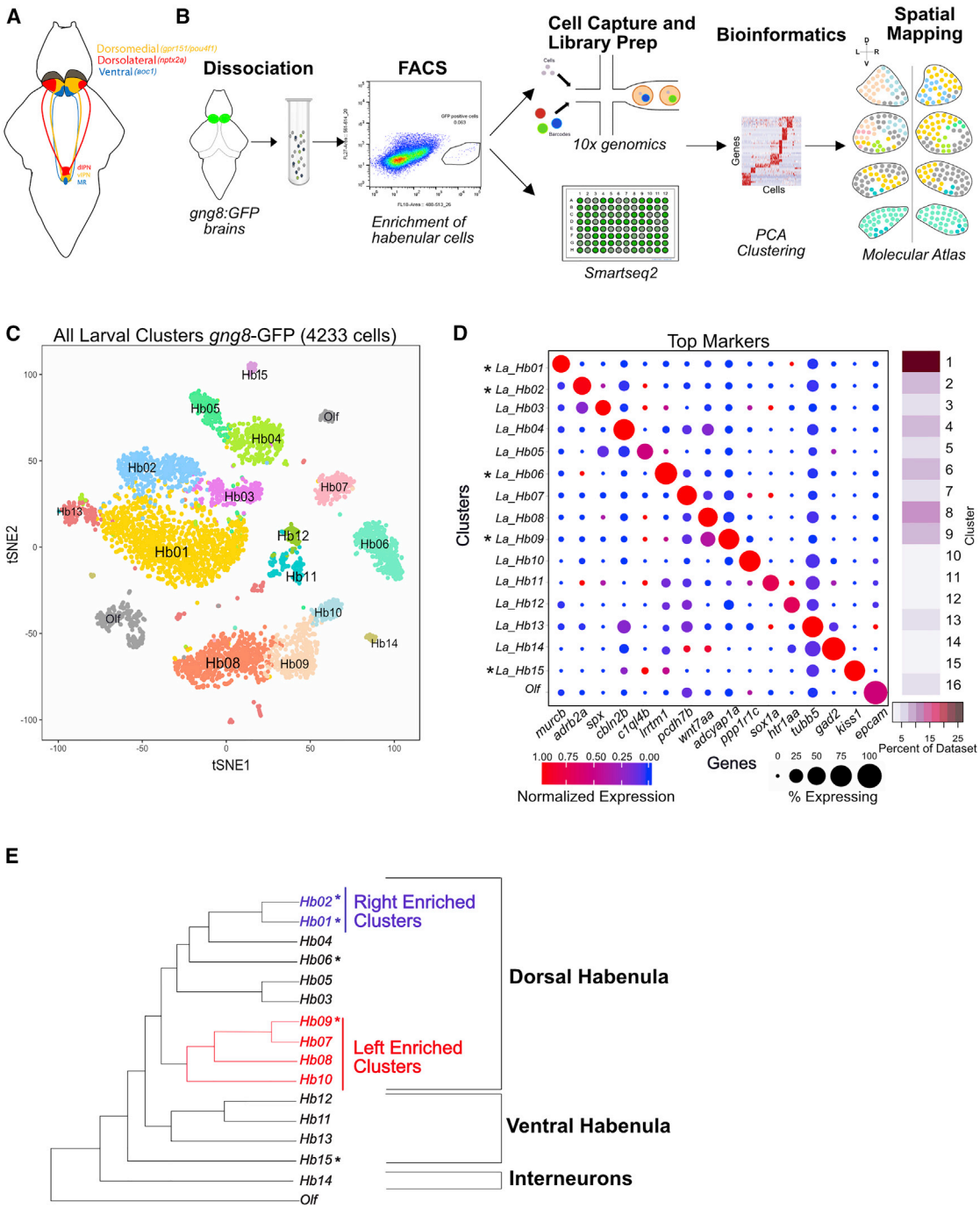

Figure 1. Unbiased Clustering of scRNA-Seq Data Identifies 15 Molecularly Distinct Neuronal Clusters in the Larval Habenula

(A) Schematic of the zebrafish habenula showing the anatomical subdivisions corresponding to the dorsomedial (orange), dorsolateral (red), and ventral (blue) regions. These subdivisions are known to have distinct gene expression patterns and functionality.

(B) Overview of the experimental strategy. Transgenic heads with *gng8*-GFP positive cells were dissected, pooled, and dissociated, followed by enrichment of GFP^+ habenular cells using fluorescent-activated cell sorting (FACS). Single-cell libraries were prepared using droplet-based droplet and plate-based Smart-seq2. Raw reads were processed to obtain a gene expression matrix (genes × cells). PCA and graph clustering was used to divide cells into clusters and identify cluster-specific markers. Validation and spatial localization was performed using fluorescent RNA *in situ* hybridization (FISH) of statistically significant cluster-specific markers (see STAR Methods).

(C) 2D visualization of single-cell clusters using t-distributed stochastic neighbor embedding (t-SNE). Individual points correspond to single cells and are color coded according to their cluster membership determined by graph-based clustering. The t-SNE mapping was only used for post hoc visualization of the clustering but not to define the clusters themselves.

(legend continued on next page)

whether these neuronal ensembles represent transcriptionally distinct neuronal types. A comprehensive definition of habenular neuronal types is therefore needed to study its development and anatomy and relate molecularly defined neuronal types to functional roles.

To address this challenge, we combined single-cell RNA sequencing (scRNA-seq) with anatomical brain registration and created a gene expression atlas composed of more than a dozen distinct neuronal types. We find that neuronal types are anatomically organized into spatially segregated sub-regions and are stable between larval and adult stages. We show that the reference atlas enables comparison of molecularly defined neuronal types with those defined by neural activity. Our approach constitutes a general framework for future studies aiming to comprehensively characterize other brain regions.

RESULTS

Isolation and Transcriptional Profiling of Single Larval Zebrafish Neurons

Since scRNA-seq had not been previously applied to zebrafish neurons, we devised and optimized a robust protocol for dissociation and capture of single neurons from the zebrafish brain. We found that successful experiments required gentle trituration, reduced processing time post-dissociation (<30 min), and minimal sort pressure during fluorescence-activated cell sorting (FACS) (STAR Methods). We sorted habenular cells using the *gng8*-GFP transgenic line [22], which selectively labels most neurons in the habenula, except for a small ventral subpopulation [23]. Heterogeneity in this subpopulation was captured using adult animals as described later.

We used two complementary scRNA-seq platforms (Figure 1B; STAR Methods): (1) massively parallel droplet based, 3′ end scRNA-seq (commercial 10× Chromium platform) [29] and (2) lower-throughput, plate-based, full-length scRNA-seq (SMART-Seq2) [30]. We obtained data from 4,365 larval cells using droplet-based scRNA-seq (henceforth droplet dataset) sequenced at a median depth of 66,263 reads per cell, and 1,152 larval cells using SMART-seq2 (henceforth SS2 dataset), sequenced at a median depth of 1 million reads per cell. Despite the low levels of RNA in zebrafish neurons (~6 times less than mouse dendritic cells that are of comparable size; Figures S1A and S1B), we detected on average 1,350 (droplets) and 3,850 (SS2) genes/cell (Figures S1C and S4A). Thus, multiple scRNA-seq platforms can be effectively applied to neurons in the zebrafish brain.

Graph Clustering Identifies 15 Transcriptionally Distinct Clusters in the Larval Habenula

To identify neuronal types, we used the droplet dataset, because cell-type identification was more robust with more cells sequenced at a shallow depth than few cells sequenced deeply (detailed analysis in Figure 4) [10]. We used standard computational pipelines to align the raw sequencing data to the zebrafish transcriptome and derive a gene expression matrix of 13,160 genes across 4,233 filtered cells (STAR Methods). To select highly variable genes, we used two approaches: (1) a variable gene selection method implemented in Seurat [31], and (2) an alternative approach that ranks genes based on deviation from a null statistical model built on the relationship between variation in transcript counts and mean expression per cell (STAR Methods).

We used principal component analysis (PCA) on a gene expression matrix across 1,436 variable genes and identified 36 statistically significant principal components PCs ($n = 36$, $p < 0.05$). These PCs were used to build a k-nearest neighbor graph of the cells, which was then partitioned into 14 transcriptionally distinct clusters using smart local moving community detection algorithm [32] as implemented in the Seurat R package [31]. Two of these clusters held additional heterogeneity and were further partitioned using iterative clustering (Figure S1G). The resulting 16 clusters were visualized in two dimensions using t-distributed stochastic neighborhood embedding (t-SNE) (Figure 1C) and evaluated for differential gene expression to identify cluster-specific markers (Figure 1D) [10, 32, 33].

Of the 16 clusters identified in our analysis, 15 were habenular neuronal types (Hb01–Hb15) as they robustly expressed *gng8* and other habenular genes (Figure S2A). We also identified a small sub-group of olfactory placode cells (*Olf*) that are labeled by the *gng8*-GFP line, based on their expression of *epcam*, *calb2a*, and *v2rl1* (Figure 1E) [34]. This provides an internal control and demonstrates the strength of scRNA-seq to identify contaminant types and remove them from further analysis.

To determine whether clusters corresponded to new or previously described neuronal types, we identified a host of markers for each cluster (Table S1; Figure S1L). The majority of clusters were defined by newly identified markers (Figure 1D). We also determined the relationship between these putative neuronal types using a dendrogram constructed on the variable genes across the dataset (Figure 1E). Some clusters recovered in our data comprise <1% of the dataset (Figure 1D, side bar), underscoring the advantages of oversampling cells in resolving rare types. Indeed, downsampling analysis on the droplet data suggests that we have reached saturation, but that reducing the number of cells by 20% would lead to recovery of fewer clusters (Figures S1H–S1K). These results demonstrate that the small number of neurons in larval habenula can be partitioned into 15 distinct clusters when the cells are sampled at a high frequency.

Most Previously Described Region-Specific Genes Are Expressed Broadly across Multiple Neuronal Clusters

To understand how our cluster-specific markers relate to previously described habenular genes, we examined the expression

(D) Gene expression profiles (columns) of select cluster-specific markers identified through differential expression analysis (DEA) of previously known (labeled with an asterisk [*]) and new habenular types (rows). Bar on the right displays the percentage of total dataset represented in every cluster, showing the abundance of each cell type found by clustering analysis.

(E) A dendrogram representing global inter-cluster transcriptional relationships. The dendrogram was built by performing hierarchical clustering (correlation distance, average linkage) on the average gene-expression profiles for each cluster restricting to the highly variable genes in the dataset.

See also Figure S1 and Table S1.

patterns of these spatially localized genes among our clusters (Figures 2 and S2A). We found three major patterns.

First, some known genes show a near perfect overlap with single clusters and were also independently identified as cluster-specific markers by our analysis. For example, *adcyap1a*, a known "left-only" marker [18] is specific to cluster Hb09. Similarly, known ventral genes such as *aoc1* [17, 18, 22] and *kiss1* [35] are specific to cluster Hb15 (Figure 2A). For such neuronal types, we nominated a host of additional markers (e.g., Hb06 [*pnoca*, *pou3f1*], Hb09 [*igf2a*, *adra1d*, *tacr2*], Hb15 [*csrp2*, *crip1*, *cabp7*, *cdh13*, *wnt11r*]) and confirmed their spatially restricted expression patterns (Figures 2E–2G).

Second, some genes that were known to mark subdomains within the dorsal habenula spanned a few clusters. For instance, *tac3a*, a previously described marker [25], is expressed in multiple clusters but at much higher levels in Hb01 and Hb02 (Figure 2A). Cluster-specific markers for Hb01 (*murcb*) and Hb02 (*adrb2a*) seemed to subdivide the high *tac3a*-expressing neurons in the habenula (Figures 2A–2D).

Third, most genes previously reported to have regional expression patterns within the habenula were expressed across multiple clusters [17, 23–25, 35] (Figure S2A). For example, *gpr151*/*pou4f1*, which together form classic dorsomedial markers [19, 36], and *nptx2a*, a dorsolateral marker [18], were expressed in majority of clusters, albeit at different levels (Figure S2A). We detected higher expression of *nptx2a* in the left habenular clusters (Figure S2A), confirming the previously observed over-representation of lateral identity in the left habenula [24]. We validated the overlap of these classic markers with multiple clusters by RNA-fluorescence *in situ* hybridization (FISH) (Figure S2B), demonstrating that individual genes reported to be spatially restricted could span multiple neuronal subtypes.

Among our newly identified markers, we found (1) markers that are expressed exclusively in the cluster of interest ("digital"), and (2) markers that display 2- to 3-fold enrichment in the cluster of interest ("analog"). To compare the specificity of marker genes, we computed their area under the precision recall curve (AUCPR) as a quantitative measure of "cluster specificity" (see STAR Methods). Digital markers such as *aoc1* displayed AUCPR values greater than 0.8 (Figure S2C), whereas analog markers such as *tubb5* exhibited lower AUCPR values (0.55–0.7). We found that considering pairs of analog markers affords higher specificity in defining a cluster. For instance, *pou3f1* and *pnoca* together localize Hb06 better than each does individually (Figure 2A). Therefore, we only used single markers with AUCPR >0.7 to spatially localize clusters of interest.

Taken together, these results provide novel analog and digital markers for the five clusters that were readily defined by expression of known genes and describe their *in vivo* spatial localization. Strikingly, the majority of previously described habenular genes are broadly expressed over multiple clusters, limiting their utility as markers for transcriptionally distinct neuronal types.

Analysis and Validation of Previously Uncharacterized Habenular Neuronal Types

The remaining 10 of 15 clusters expressed marker genes that to our knowledge have not been previously described in the zebrafish habenula. We hypothesized that these clusters corresponded to potentially novel neuronal subtypes and performed RNA-FISH with cluster-specific markers to validate them and determine their spatial localization (Figure 3). We also utilized the gene expression dendrogram (Figure 1E) to relate them to "known" neuronal types described earlier. Based on spatial localization, we found three major categories of neuronal subtypes.

First, we identified three new "left-enriched" clusters of neurons—Hb07(*pcdh7b*$^+$) and Hb08(*wnt7aa*$^+$), Hb10(*ppp1r1c*$^+$)—all of which were closely related to one another and to the left-only neuronal type Hb09 (*adcyap1a*$^+$) (Figure 1E). All of these clusters also expressed another known left-only marker, *nrp1a* (Figure S2A) [24]. Hb08 (*wnt7aa*$^+$) and Hb10 (*ppp1r1c*$^+$) neurons were localized more dorsally in the left habenula than Hb07 (*pcdh7b*$^+$) (Figure 3A).

Second, we identified three posterior L-R symmetric habenular neuronal types (Figure 3B). Dorsally located Hb04 was characterized by the expression of *cbln2b*, a less-studied member of the cerebellin genes, some of which are important for synaptic plasticity [37]. Ventrally located *pyya*$^+$ neurons were subdivided into Hb11 (*cpne4a*$^+$) and Hb12 (*htr1aa*$^+$). Corresponding to their low proportion by scRNA-seq, RNA-FISH showed that Hb11 and Hb12 are rare, composed of 4–6 neurons *in vivo*.

Third, we found four rare neuronal types, each comprising less than 5% of the cells in our dataset. Hb03(*spx*$^+$) and Hb05(*c1ql4b*$^+$) form rare populations that seem to be distributed in a non-regionalized manner (Figures 3C, upper panels). Hb13 is a cluster of immature neurons in the medial ventral habenula and lining the ventricular zone, characterized by the expression of *tubb5* and a host of ribosomal proteins (Figure 3C, lower right panel) [38]. Rarest among these four types were GABAergic neurons in the dorsal habenula (Figures 1D and 3C, lower left panel) characterized by the expression of *gad1b*, *gad2*, and the GABA transporter *slc32a1* and corresponding to 2–3 neurons *in vivo*.

Together, these results provide validation and spatial localization for the 10 novel neuronal types identified by our single-cell analysis and demonstrate a general trend for regionalization of neuronal types within the habenula. Moreover, transcriptional proximity was reflected by spatial proximity *in vivo*, suggesting that developmental patterning of molecularly related neuronal types occurs in a spatially restricted manner.

Computational Image Registration Generates a Spatial Map of Neuronal Types in the Habenula

To explore the localization of neuronal types in relation to one another, we created a consolidated spatial map of neuronal-type-specific markers in the habenula (Figures 3D and 3E; Movie S1). We used computational image registration to morph RNA-FISH signals across multiple zebrafish larvae onto a single reference based on the total ERK (tERK) antibody stain [39–41] (Figures S3A and S3B) resulting in a reference spatial map of the habenula (Movie S1).

Our map demonstrates that a majority of habenular types were regionalized either along the dorsoventral, medio-lateral, or left-right axis, suggesting that habenular types can be defined not only by their transcriptomes, but also by distinct spatial positions (Figure 3E; Movie S1). Eleven types were located more dorsally in the habenula; 8 of them seem to be regionalized: Hb01/Hb02 were right enriched or exclusive, Hb07/Hb08/Hb09/Hb10 were

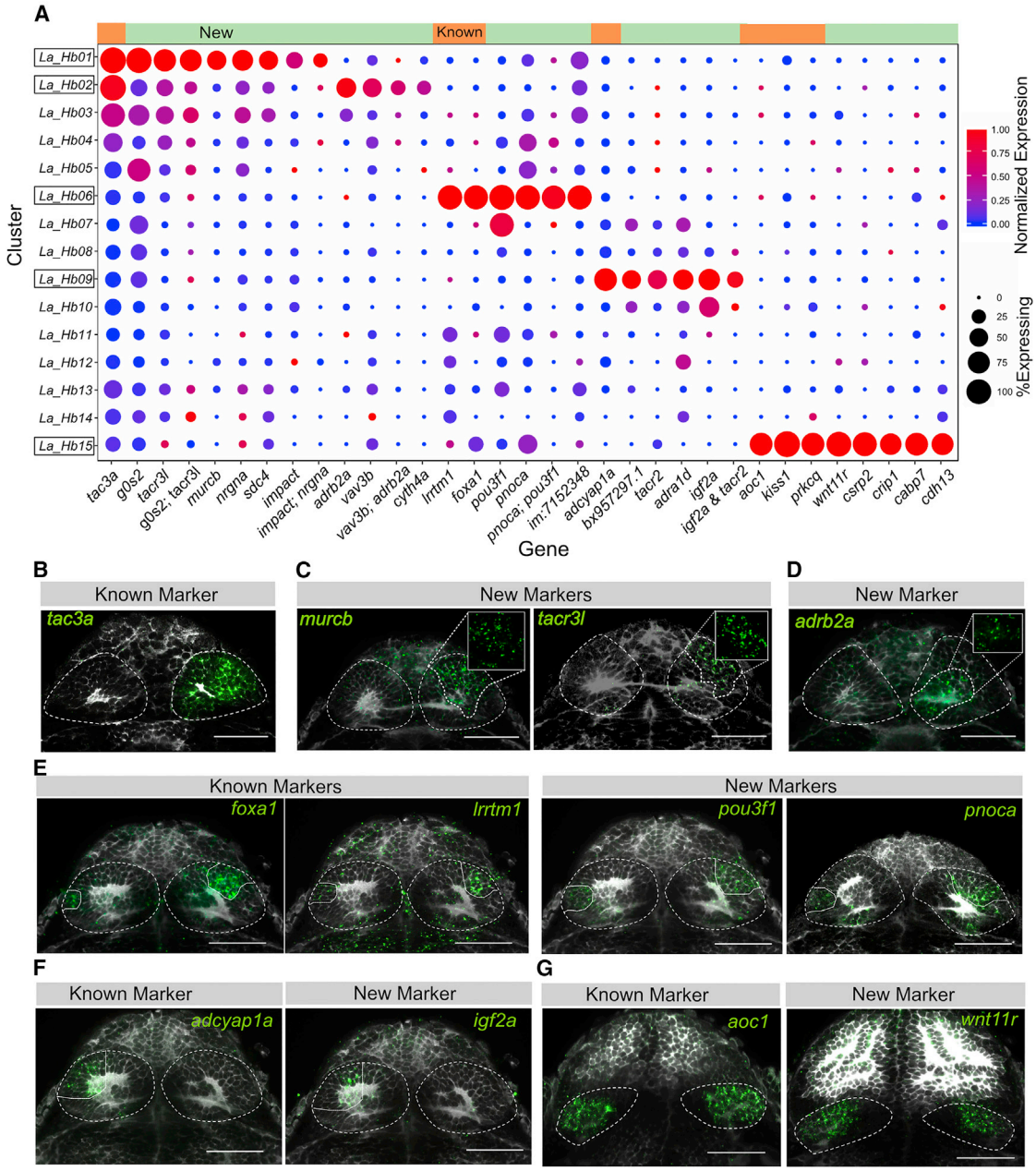

Figure 2. Validation and Spatial Distribution of Previously Described Neuronal Types along with Identified Novel Markers

(A) Expression profiles of known and novel habenular marker genes that are specific or enriched in the five clusters displaying previously described gene expression signatures. Green bar on top represents new markers, and orange bar represents known markers.

(B–G) *In vivo* expression patterns of known and novel marker genes that are enriched in clusters harboring previously characterized habenular genes (Hb01, Hb02, Hb06, Hb09, and Hb15). Each type was characterized by both previously described markers, and new markers found from single-cell analysis. RNA-FISH (green) was performed with a total-Erk (pale gray) co-stain for registration (see Figure 3). In some cases, a non-linear filter (gamma = 0.3) was applied to the total-Erk (gray) channel to aid visualization of the *in situ* signal (green).

(B–D) FISH labeling of (B) previously known marker (*tac3a*) and new markers for (C) Hb01 (*murcb*, *tacr3l*) and (D) Hb02 (*adrb2a*) found by single-cell analysis. Insets show regionalized expression of the gene without total-Erk.

(E) FISH labeling of new markers *pou3f1* and *pnoca* enriched in the *lrrtm1*$^{+}$ and *foxa1*$^{+}$ cluster Hb06.

(F) FISH labeling of new marker *igf2a enriched in adcyap1a*$^{+}$ left-only cluster Hb09.

(G) FISH labeling of new marker *wnt11r* specific to the *aoc1*$^{+}$ ventral habenular cluster Hb15. Scale bars indicate 50 μm.

See also Figures S2 and S3, Table S1, and Movie S1.

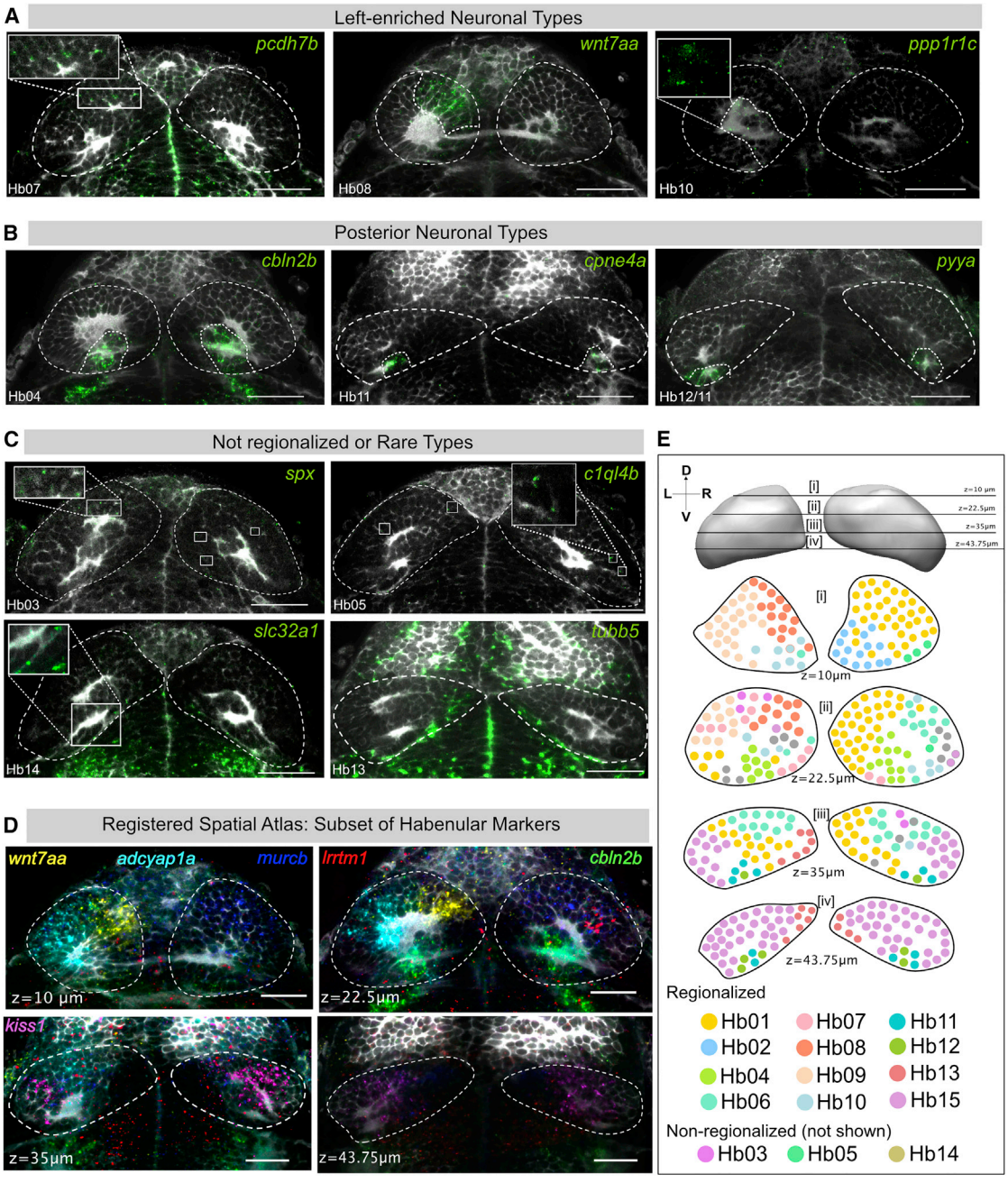

Figure 3. Validation and Spatial Distribution of 10 Novel Habenular Neuronal Types

(A–C) RNA-FISH (green) was performed for specific markers for novel clusters. (A) Left-enriched clusters: Hb07 (*pcdh7b*), Hb08 (*wnt7aa*), Hb10 (*ppp1r1c*); (B) posterior habenular clusters: Hb04 (*cbln2b*), Hb11 (*cpne4a*), Hb12/11 (*pyya*); (C) non-regionalized or rare neuronal types: Hb03 (*spx*), Hb05 (*c1ql4b*), Hb14 (*slc32a1*), and Hb13 (*tubb5*), each overlaid with a total-Erk co-stain (pale gray) for registration. In each case, representative habenular slices with expression are shown. Full stacks are available through a linked website (see Data and Software Availability).

(D) Slices through the registered reference habenula simultaneously showing six marker genes that are expressed in a regionalized pattern: *wnt7aa* (La_Hb08), *adcyap1a* (La_Hb07), *cbln2b* (La_Hb04), *murcb* (La_Hb01), *lrrtm1* (La_Hb06), *gpr139* (La_Hb15).

(E) Schematic of representative transverse slices through the habenula displaying rough spatial co-ordinates of previously described as well as new neuronal types found by single-cell analysis. Cells are color coded based on their identity in the t-SNE plot (see Figure 1C). Depth is indicated by the z slice in microns. The sectioning extends from z = 0 µm (dorsal) and z = 75 µm (ventral). Only regionalized markers are represented. Schematic is a simplified representation of an accompanying stack of registered habenular markers overlaid onto one another (see Movie S1). Scale bars indicate 50 µm.

See also Figure S3, Table S1, and Movie S1.

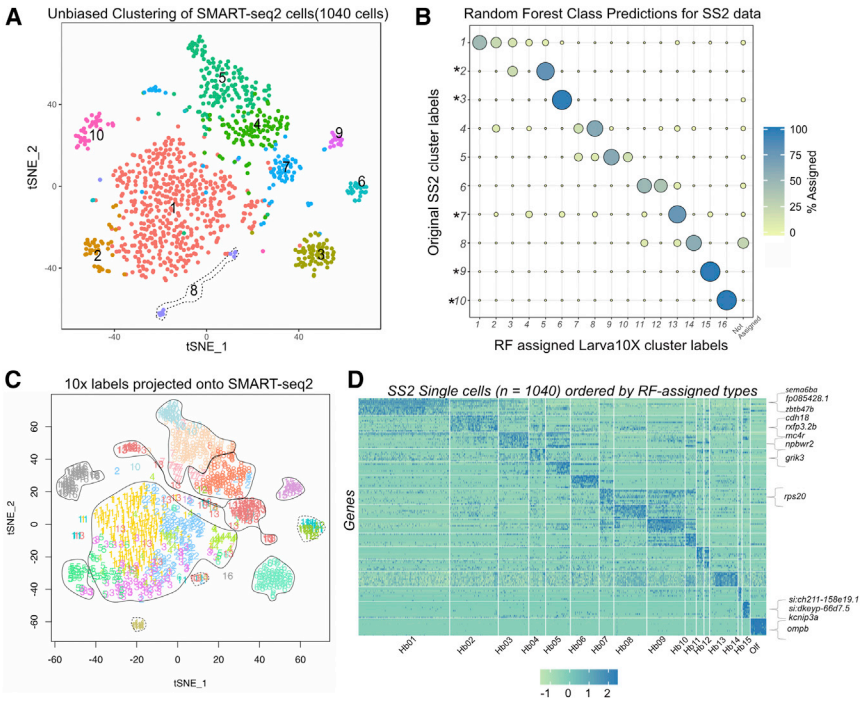

Figure 4. Correspondence of Larval Habenular Neuronal Types and Their Molecular Identities between the Droplet and SMART-seq2 Datasets

(A) t-SNE visualization of single-cell clusters obtained by clustering of the SMART-seq2 (SS2) data.

(B) Dot plot (confusion matrix) showing the proportion of cells in each SS2 cluster (rows) that were classified to droplet clusters (columns) using a multiclass random forest classifier (RF). A cell was assigned to a droplet cluster label if >15% of the decision trees in the RF classifier contributed to the majority vote (given that there are 16 classes, 6.25% vote would constitute a majority). *SS2 clusters in which greater than 70% of the cells of the cluster maps to single-droplet clusters.

(C) Same as (A), but where each cell is annotated according to its RF assigned droplet cluster label. Rough demarcations of the SS2 clusters as in (A) are sketched.

(D) Top 10 differentially expressed genes in each habenular type computed using a post hoc test on the SS2 data based on the RF-assigned cluster label as in (C). Highlighted on the right are anecdotal examples of genes that were not detected among the top 15 differentially expressed genes in the corresponding droplet clusters.

See also Figure S4.

left-enriched or exclusive, Hb04 and Hb06 was L-R symmetric in the dorsal habenula. Four types were located more ventrally, of which Hb11 and Hb12 were posterior ventral populations, Hb15 occupied a large portion of the ventral habenula, and Hb13 formed a germinal zone along the medial region of the ventral habenula. In summary, our fluorescent *in situ* atlas provides the first spatial map of the 15 known and novel neuronal types in the zebrafish habenula.

Neuronal Types in the Larval Habenula and Their Molecular Signatures Are Robustly Reproduced in Full-Length, Deeply Sequenced Libraries

Because zebrafish neurons contain less RNA than other cell types—including of comparable size—analyzed using scRNA-seq (Figures S1A and S1B) [10, 42], we asked whether we could derive a better classification by sequencing these neurons at a greater depth. To explore this possibility, we prepared 1,152 SMART-seq2 (SS2) libraries using cells sorted from the *gng8*-GFP transgenic line [30] and sequenced them at a median depth of 1 million reads per cell (~25-fold deeper than the droplet data; Figures S4A and S4B), resulting in 3,850 genes/cell, (~3-fold more than the droplet data).

An independent clustering of 1,040 quality-filtered SS2 cells revealed only 10 clusters (Figure 4A), fewer than the droplet data. We hypothesized that the lower number of cells in SS2 dataset led to merging of closely related clusters. To evaluate the correspondence between droplet and SS2 clusters, we trained a multiclass random forest classifier (RF) on the cluster labels of the droplet dataset (Figure S4I) and used it to map all the SS2 cells onto droplet-based labels [10, 43]. We observed that 5 out of 10 SS2 clusters mapped 1:1 with single-droplet clusters (Figure 4B). Each of the four remaining SS2 clusters mapped to multiple (typically 2–3) droplet clusters (Figure 4B). By labeling each cell on the t-SNE plot with RF assigned cluster labels, we observed additional sub-structure in the merged SS2 clusters that was masked in unsupervised clustering (Figure 4C). This co-clustering occurs in cases where clusters are closely related (Figure 1E) but not highly represented in the dataset (e.g., Hb05-Hb03, Hb02-Hb01-Hb04, Hb07-Hb08). These results are also consistent with the recovery of fewer and less pure clusters in the downsampled droplet dataset (Figures S1H–S1K).

Next, we asked whether the higher number of genes/cell identified in SS2 data enabled the identification of novel cluster-specific markers. To this end, we examined genes that were robustly detected in the SS2 data but not in droplet data (Figures S4J, S4K, and S4L, red) but found that they were expressed across multiple clusters and were uninformative for cell-type classification (Figure S4M; STAR Methods). Using differential gene expression analysis on the RF-assigned cell labels, we identified a small number of novel cluster-specific markers that were not identified in the droplet dataset (Figure 4D, highlighted along the heatmap).

Taken together, these results demonstrate a remarkable consistency of types and markers discovered by two different scRNA-seq platforms. Also, consistent with earlier work [10], these results show that cell-type identification is best served by distributing a given number of reads over a large number of cells.

Neurons in the Adult Habenula Retain the Molecular Identity of Larval Types

The habenula undergoes significant growth, morphogenesis, and functional maturation from developing larvae to mature adults (Figure S5I, left). For example, several behaviors mediated

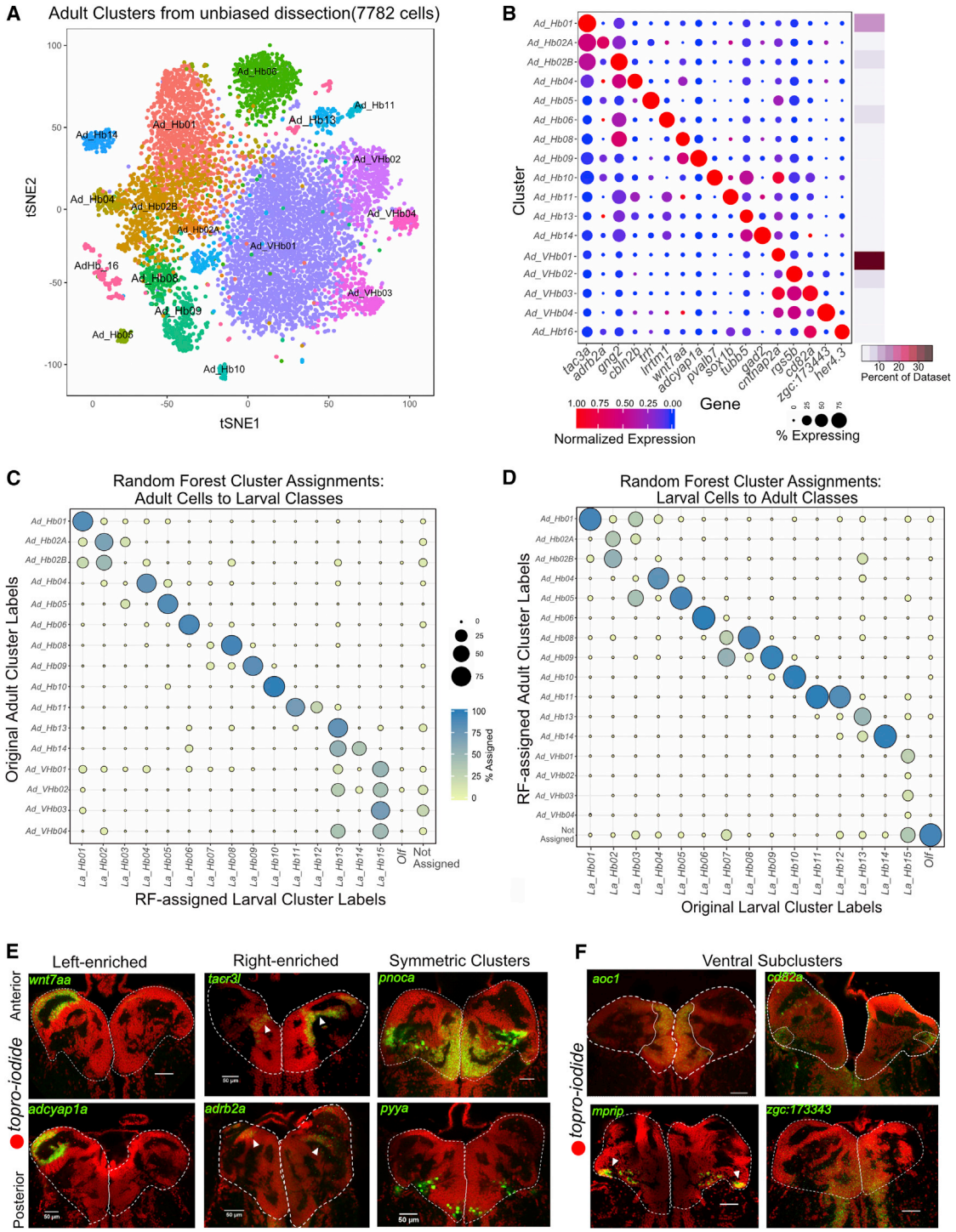

Figure 5. Comparative Analysis of Habenular Neuronal Types between Larval and Adult Stages

(A) t-SNE visualization of adult single-cell clusters obtained by clustering of the adult dataset. Clusters have been labeled post hoc after comparison to the larval dataset (see Figures 5C and 5D).

(B) Gene expression profiles (columns) of select cluster-specific markers identified through differential expression analysis (DEA) across all adult clusters. Bar on the right displays percentage of total dataset represented in every adult cluster, showing the abundance of each cell type found by clustering analysis.

(C) Dot plot (confusion matrix) showing the proportion of *gng8*$^{+}$ cells in the adult dataset (rows) that were classified to larval cluster labels (columns). Each adult habenular type was assigned to a larval cluster label if >15% of the trees in the RF model contributed to the majority vote. Proportion of cells in each row should add to a 100%.

(legend continued on next page)

by habenular neuronal subpopulations such as aggression are only displayed by adult fish, in which the number of habenular neurons also increases dramatically [18, 19]. Furthermore, the larval dataset was generated from a transgenic line using FACS and may have missed rare populations not labeled by the *gng8*-GFP line. To assess the conservation and retention of neuronal types from larva to adult fish (1 year old) and to capture cells that were not labeled by the transgenic line, we dissected whole adult habenulae and performed droplet scRNA-seq (STAR Methods). After quality filtering, we obtained 7,782 single-cell profiles at a median depth of ~96,000 reads and 709 genes per cell (Figures S5A and S5B). Using the same clustering approach as before, we detected 17 clusters and enriched markers (Figures 5A and 5B) and labeled them post hoc by comparison to the larval clusters (see below).

To systematically compare the clusters between larva and adult, we used a RF model trained on either dataset to map gene expression signatures between the two datasets (Figure 5C (trained on larva) and Figure 5D (trained on adult)). Since the larval dataset was generated by cellular sorting based on the *gng8*-GFP line, we restricted our analysis to the high *gng8*$^{+}$ cells in the adult dataset. Using the RF model, we then classified each high *gng8*$^{+}$ adult cell (Figure S5F) into one of the larval cluster labels (Figure 5C). Surprisingly, we found that 9 out of the 16 adult habenular clusters mapped 1:1 to single larval habenular clusters (Figure 5C). The left-right spatial organization of some clusters was also roughly preserved (Figure 5E).

We also found that some larval clusters map to multiple adult clusters. For instance, La_Hb02 (La = Larval) split into Ad_Hb02A and Ad_Hb02B (Ad = Adult). Upon interrogating the differences between Ad_Hb02A and Ad_Hb02B further, we found that certain genes such as *nebl* are selectively expressed in Ad_Hb02B, whereas others such as *rac2* are in Ad_Hb02A (Figure S5G). Furthermore, larval ventral cluster La_Hb15 mapped to multiple adult types, all of which are ventral (Ad_VHb01-04) as found by RNA-FISH for differentially expressed markers *cntnap2a*, *mprip*, *cd82a*, and *zgc:173443* (Figure 5F). The spatial localization of these ventral clusters was found to be consistent with previously described [17] morphogenetic changes that occur in the habenula between larval and adult stages (Figure S5I).

This multi-mapping among ventral clusters was likely caused by incomplete labeling of ventral habenula by the *gng8-GFP* line, which was used to capture cells in larval dataset. In particular, ISH revealed that two of the adult ventral type markers were expressed in a spatially restricted pattern in the larval ventral habenula (Figure S5D). We also found a small population of neuronal progenitors (*her4*$^{+}$, *fabp7a*$^{+}$, *mdka*$^{+}$) in the medial ventral habenula (Figures 5B and S5E), in a similar location as the immature *tubb5*$^{+}$ (Figure 3D) neurons in the adult dataset.

Taken together, these results demonstrate that despite significant growth and functional maturation between larvae and adults, a substantial number of neuronal types in the habenula remain largely constant.

Neuropeptidergic Signaling, Neurotransmission, and Neuroexcitability among Habenular Neuronal Types Are Highly Diverse

Previous studies have used ISH or immunostaining to assess the expression of various neuropeptidergic and neurotransmitter genes in the habenula [22, 23], but a comprehensive expression profile of these genes is not available. Using the scRNA-seq dataset, we assessed the expression profiles of these genes among the different neuronal types in the larval (Figure 6) and adult (Figure S6) habenula.

We found that a large number of neuropeptides are specific to a small number of neuronal types (Figures 6A and S6A). For example, *spx*, *trh*, *adcyap1a*, *tac1*, *agrp*, *kiss1*, *npy*, *galn*, and *penka* were all expressed in only one habenular type each, whereas *pyya*, *pyyb*, *pdyn*, *pnoca*, *sst1.1*, *tac3a*, and *cckb* were enriched in 2–4 neuronal types. In addition, co-expression of multiple neuropeptides was a common feature among habenular neuronal types. For instance, *spx*, which acts as a satiety factor, and *pyyb*, which has been implicated to be an anorexigenic factor, were co-expressed in the homologous clusters in both larvae and adults, respectively [44]. Conversely, we examined the expression profile of all detectable neuropeptide receptors. In some cases, the same neuronal type produces a neuropeptidergic signal and expresses its cognate receptor, suggesting autocrine signaling. For instance, *kiss1* and its receptors *kiss1rb* and *kiss1ra* are co-expressed in ventral habenular clusters (Figures 6A and S6A).

Next, we analyzed the expression of genes essential to signal transduction in neurons. As previously observed [45], a large proportion of habenular neurons are glutamatergic, as reflected in the broad expression of glutamate transporters *slc17a6a* and *slc17a6b* (Figure 6B). However, the habenula also contains a small population of GABAergic neurons (Figure 6B). Hb01 through Hb05 are also cholinergic and express the choline transporter *slc5a7a* (Figure 6B). Cholinergic transmission was largely absent in left-enriched neuronal types consistent with previous studies [22]. Similarly, some neurotransmitter receptor subunits such as *grm8b*, *grm2*, and *gria2b* are enriched in one or a few clusters (Figure 6C). Calcium channels such as *cacng2a*, *cacna1g*, and *cacna1ba* are also expressed in a type-specific manner, as are potassium channel subunits such as *kcnab1b*, *kcnf1b*, *kcnh6a*, and *kcnd3* (Figures 6D and 6E). We found a similar distribution of these functionally relevant genes in the adult habenula (Figures S6A–S6F). Collectively, our data show that despite being a small region, the habenula shows a remarkable diversity in expression of genes that directly influence the functional and electrophysiological properties of individual neurons.

(D) Dot plot (confusion matrix) showing the proportion of larval cells (rows) that were classified to cluster labels of the *gng8*$^{+}$ cells in the adult dataset (columns). Each adult habenular type was assigned to a larval cluster label if >15% of the trees in the RF model contributed to the majority vote. Proportion of cells in each column should add to a 100%. This training on the adult dataset was performed to validate the robustness of the RF analysis.

(E) FISH validation and localization of select dorsal habenular cluster markers.

(F) FISH validation of the genes that are expressed in all ventral clusters (*aoc1*) and across three other ventral sub-clusters (*cd82a*, *mprip*, and *zgc:173443*). See also Figure S5 and Table S2.

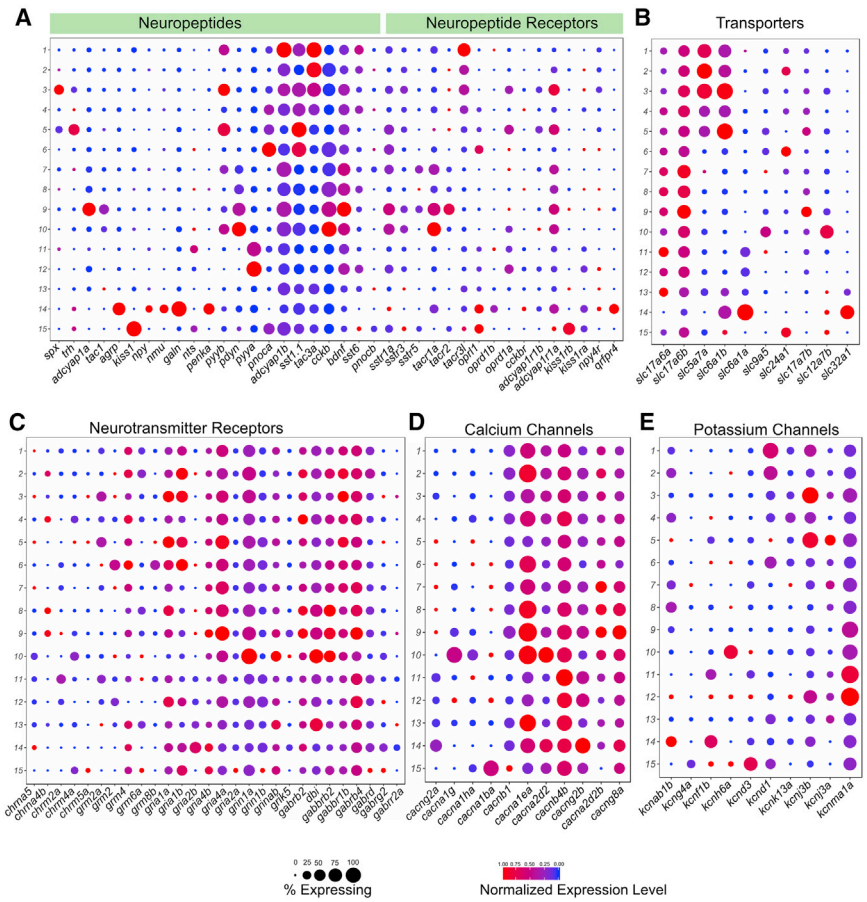

Figure 6. Divergent Expression Patterns of Functionally Relevant Genes among the Larval Habenular Neuronal Types

(A–E) Gene expression profiles of select functionally relevant genes among larval habenular types visualized in the form of a dot plot. Representation is as in Figure 1D. (A) Neuropeptides and neuropeptide receptors; (B) transporters; (C) neurotransmitter receptors; (D) calcium channels; (E) potassium channels. Only genes expressed in >20% of cells in at least each habenular type are shown.

See also Figure S6.

DISCUSSION

We used two scRNA-seq platforms, integrative computational analysis, and brain registration to build and validate a comprehensive atlas of neuronal types in the larval and adult zebrafish habenula. Our study provides six main advances. First, we devised a robust protocol for the dissociation and capture of single neurons from the zebrafish brain. Second, we found that comprehensive identification of neuronal types by scRNA-seq can be achieved by high cell-sampling coverage of a small brain region. Third, we discovered thirteen new neuronal types and identified fine-grained spatial subdivisions in the habenula. Fourth, we discovered dozens of new marker genes that define habenular neuronal types. Fifth, we found that diverse neuronal types are largely retained from larva to adult. Sixth, we showed that the reference atlas enables comparison of molecularly defined neuronal types with those defined by neural activity. Taken together, our study creates a resource for future studies on habenular development and function and provides a technological framework for the characterization of other brain regions.

Functional Assignment onto Molecularly Defined Neuronal Types

Finally, we began to explore whether and how functional responses of the habenula are distributed among these transcriptionally distinct neuronal types. To this end, we performed a proof-of-principle experiment to determine whether we could use neuronal-type-specific markers and the reference habenular atlas (Figure 3E; Movie S1) to map responses to specific stimuli among the molecularly defined neuronal types. We exposed fish to electric shocks and assessed upregulation of the immediate early marker gene *cfos* in specific neuronal types. We observed localized upregulation of *cfos* expression in specific sub-regions within the habenula in shocked animals (Figure 7A). We registered the *cfos* RNA-FISH signals onto our reference habenular map and detected overlap within the domains of expression of left habenular Hb09 (*adcyap1a*$^{+}$), posterior habenular Hb04 (*cbln2b*$^{+}$), and largely within the ventrolateral population (*mprip*$^{+}$) (Figures S7A, 7A, and 7B). Double ISH for *mprip* and *cfos* showed a regional overlap between the *mprip*$^{+}$ and *cfos*$^{+}$ cells in both larva (Figure 7C) and adult (Figure 7D; Movie S2). Together, these results show that neuronal ensembles in the ventrolateral habenula comprise a large proportion of cells responsive to aversive electric shocks and demonstrate the utility of the habenular atlas to link functional responses to molecularly defined neuronal types.

Single-Cell Analysis of the Zebrafish Brain

Although scRNA-seq is now well established, applying it to zebrafish neurons presents certain technical challenges. Our work establishes critical conditions for future scRNA-seq in the zebrafish brain. We provide a robust dissociation and sorting-based cell capture protocol for zebrafish neurons (STAR Methods), which were found to have comparatively less RNA than other cell types. Consistent with previous studies, we also found that transcriptional signatures required to classify cell types can be identified by low coverage RNA-seq [10]. Therefore, most of the additional genes detected in the deeper SMART-seq2 dataset were uninformative for cell-type classification (Figure S4M).

Comprehensive Cell-Type Identification and Spatial Mapping in the Habenula Facilitates Functional Studies

Based on scRNA-seq on larva and adults, we found that the habenula is composed of at least 18 distinct neuronal subsets. While larval ventral heterogeneity needs to be explored

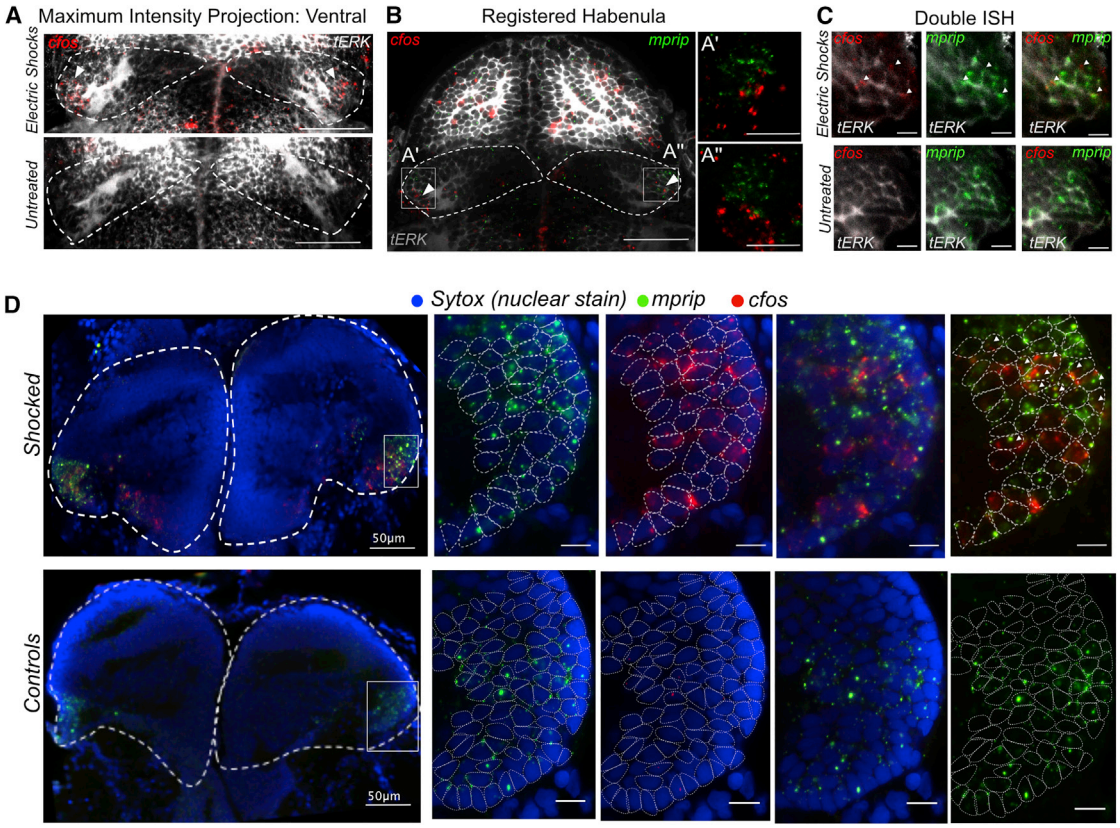

Figure 7. Noxious Electric Shocks Activate a Sub-population of Neurons in the Ventro-lateral Habenula Labeled by *mprip*

(A) ISH analysis of *cfos* expression in the habenula 30 min after exposure to electric shocks. (Scale bars represent 50 μm.)

(B) Registration of *cfos* signals to habenular molecular atlas reveals co-regionalization with the *mprip*$^+$ ventrolateral population. (Scale bars represent 50 μm).

(C) Double ISH for *c-fos* and *mprip* (marker for ventrolateral neuronal type) showing a co-localization of *cfos*$^+$ and *mprip*$^+$ domains in the larval habenula in response to electric shocks. (Scale bars represent 10 μm).

(D) Double ISH of *cfos* and *mprip* showing the conservation of electric shocks-induced *cfos* responses in *mprip*$^+$ ventro-lateral neuronal type in the adult habenula. Nuclei borders are demarcated in the zoomed in panels on the right using dotted circles. (Scale bar represents 10 μm unless otherwise stated).

See also Figure S7 and Movie S2.

genome-wide using RNA-seq approaches, our two-time-point scRNA-seq and *in situ* analysis has allowed us to describe the majority of the neuronal types in the habenula. For each of these neuronal types, we found dozens of novel molecular markers. Whole-brain ISH showed that some of these markers are exclusively expressed within habenular neuronal subsets, making them good candidates for generating reporter lines (Figure S3C).

We also used RNA-FISH and image registration to spatially localize neuronal types, a key step in linking molecular profiles to physiological and behavioral features. We found that 15 neuronal subsets are highly regionalized to habenular sub-regions (Figures 3L and 5F). This arrangement is similar to regionalization observed in the hippocampus [46] but in contrast to the organization in the retina where different cell types are intermixed within the same spatial location [47].

Furthermore, we found that previously demarcated anatomical sub-regions, dHbM (*pou4f1*$^+$, *gpr151*$^+$), dHbL (*nptx2a*$^+$), and vHb (*aoc1*$^+$) harbor multiple transcriptionally distinct neuronal subsets. Previous studies have shown that these distinct sub-regions send efferent projections to distinct anatomically separated sub-regions of the downstream interpeduncular nucleus (IPN) and raphe nucleus [15]. Our study raises the possibility of a finer topography of efferent projections of transcriptionally distinct neuronal subsets into finer sub-regions of downstream targets.

We also found a large diversity of neuropeptidergic genes in the habenula, which may shed light into its unexplored functional roles. For instance, a number of peptides that are involved in food intake regulation such as *cckb*, *pyya*, *pyyb*, and *spx* are shown to be robustly expressed in certain sub-clusters of habenular cells, indicating that the corresponding neuronal types may be important for regulating food intake. Furthermore, a subset of the *pyya* neurons are positive for *htr1aa*, a serotonin receptor whose expression is known to be affected by anorexigenic drugs [48].

Therefore, our comprehensive list of neuronal types along with dozens of marker genes and their spatial map will be a valuable resource for the study of habenular development and function in normal and pathophysiological conditions.

Neurons in the Adult Habenula Retain the Molecular Identity of Larval Types

Cell-type identification should distinguish between stable cell types and transient cell states as transcriptional cascades in

individual neurons may change in response to a variety of different stimuli such as neural activity, neuropeptides, hormones, or developmental signals. Our two-time-point study design enabled us to observe the remarkable congruence of habenular subtypes between the developing 10-day-old larval and the adult brain, suggesting that these signatures represent stable molecular identities. We also found that the localization of neuronal types in the adult habenula is consistent with the complex morphogenetic changes in the habenula between larva and adult wherein the ventral cells migrate inward from lateral to medial positions (Figures S5H and S5I) [17].

A number of habenula-dependent behaviors such as fear responses and aggression arise later in development in juvenile or adult zebrafish [18, 19, 49]. In the absence of major changes in molecular cell-type diversity, what circuit mechanisms account for alterations in behavioral capacities during development? An attractive hypothesis is that habenular input-output relationships change between the two time points. For example, habenular outputs may diverge into more downstream regions to mediate a diverse set of behaviors in adults. A detailed investigation of the development of habenular inputs and outputs will be required to address this question.

Mapping the Transcriptionally Defined Neuronal Types to Functionally Distinct Types

While cell-type classification is essential for understanding the form and function of neural circuits, an important future goal is to relate such molecularly defined neuronal types to functionally defined types [2]. In many brain regions, it is not clear whether distinct, transcriptionally defined sub-populations form functionally distinct motifs as well.

Our work suggests that the habenula contains discrete, spatially and transcriptionally segregated functional ensembles. In particular, our *cfos* data suggest that habenular responses to aversive stimuli are restricted to a few molecularly defined subsets (Figure S7), including those identified by a recent study describing the role of dorsal left habenula in recovery from electric shocks [50]. The newly identified *mprip*$^{+}$ cells in the ventrolateral habenula merit further investigation as they co-express *neurotensin*, an endogenous peptide that has been emerging to have a role in stress-induced anxiety and learning (Figure S6A) [51, 52]. Similarly, our spatial map suggests that the left-exclusive neuronal subsets Hb08 (*wnt7aa*$^{+}$) and Hb09 (*adcyap1a*$^{+}$) form light responsive ensembles, found to be lateralized in the left habenula in previous studies [26] (Figure 3E, schematic). A number of other calcium imaging studies have described spontaneous and stimulus evoked activity maps in the habenula [27, 53]. Interfacing such functional maps to our molecular map using emerging techniques such as MultiMAP [54] will allow a systematic correlation of molecular profiles with functional properties. Our cell-type catalog and gene expression atlas provide the foundation for future studies to address the relationship between habenula functions and molecular identities.

Pipeline for Comprehensive Identification of Cell Types in Other Brain Regions

The comprehensive classification of neural types is limited by the large number and diversity of cells in vertebrate brains. For example, previous scRNA-seq studies have sampled a small percentage of cells to infer heterogeneity in large regions [4, 6, 55, 56]. Our study shows that such limitations can be overcome by scRNA-seq from predefined small sub-regions at high cellular coverage. The larval zebrafish brain contains fewer than 200,000 neurons, putting its comprehensive molecular classification within reach of current technologies and creating a blueprint for cell-type diversity in the vertebrate brain.

STAR★METHODS

Detailed methods are provided in the online version of this paper and include the following:

- KEY RESOURCES TABLE
- CONTACT FOR REAGENT AND RESOURCE SHARING
- EXPERIMENTAL MODEL AND SUBJECT DETAILS
  - Zebrafish
- METHOD DETAILS
  - Cell Isolation and RNA-Seq
  - Imaging Methods
  - Image visualization
  - Computational Methods for Data Analysis
  - Functional experiments
- QUANTIFICATION AND STATISTICAL ANALYSIS
- DATA AND SOFTWARE AVAILABILITY
- ADDITIONAL RESOURCES

SUPPLEMENTAL INFORMATION

Supplemental Information includes seven figures, three tables, and two movies and can be found with this article online at https://doi.org/10.1016/j.cub.2018.02.040.

ACKNOWLEDGMENTS

This work was supported by the National Institute of Mental Health (NIMH) grant U01MH109560 (A.R. and A.F.S.). We thank members of the Schier lab, particularly Martin Haesemeyer, William Joo, Summer Thyme, and Jeff Farrell for discussion. We thank Alexandra-Chloé Villani, Monika Kowalczyk, and Xian Adiconis at the Klarman Cell Observatory for helpful advice on experimental protocols. We thank Dr. Marnie Halpern for providing the *gng8*-GFP transgenic line. We also thank the Broad Flow Cytometry Core and Genomics Platform for cell sorting and sequencing services and the Harvard zebrafish facility staff for technical support.

AUTHOR CONTRIBUTIONS

Conceptualization, S.P. and A.F.S.; Methodology, S.P. and K.S.; Software, K.S. and S.P.; Validation, S.P.; Formal Analysis, S.P. and K.S.; Library Preparation and Sequencing, S.P.; Data Curation, S.P. and K.S.; Resources, A.R. and A.F.S., Writing – Original Draft, S.P., K.S., and A.F.S.; Writing – Review and Editing, S.P., K.S., A.R., and A.F.S.; Visualization, S.P.

DECLARATION OF INTERESTS

The authors declare no competing interests.

Received: October 26, 2017
Revised: January 10, 2018
Accepted: February 15, 2018
Published: March 22, 2018

REFERENCES

1. Poulin, J.F., Tasic, B., Hjerling-Leffler, J., Trimarchi, J.M., and Awatramani, R. (2016). Disentangling neural cell diversity using single-cell transcriptomics. Nat. Neurosci. *19*, 1131–1141.
2. Zeng, H., and Sanes, J.R. (2017). Neuronal cell-type classification: Challenges, opportunities and the path forward. Nat. Rev. Neurosci. *18*, 530–546.
3. Pollen, A.A., Nowakowski, T.J., Shuga, J., Wang, X., Leyrat, A.A., Lui, J.H., Li, N., Szpankowski, L., Fowler, B., Chen, P., et al. (2014). Low-coverage single-cell mRNA sequencing reveals cellular heterogeneity and activated signaling pathways in developing cerebral cortex. Nat. Biotechnol. *32*, 1053–1058.
4. Chen, R., Wu, X., Jiang, L., and Zhang, Y. (2017). Single-cell RNA-seq reveals hypothalamic cell diversity. Cell Rep. *18*, 3227–3241.
5. Tasic, B., Menon, V., Nguyen, T.N., Kim, T.K., Jarsky, T., Yao, Z., Levi, B., Gray, L.T., Sorensen, S.A., Dolbeare, T., et al. (2016). Adult mouse cortical cell taxonomy revealed by single cell transcriptomics. Nat. Neurosci. *19*, 335–346.
6. Zeisel, A., Muñoz-Manchado, A.B., Codeluppi, S., Lönnerberg, P., La Manno, G., Juréus, A., Marques, S., Munguba, H., He, L., Betsholtz, C., et al. (2015). Brain structure. Cell types in the mouse cortex and hippocampus revealed by single-cell RNA-seq. Science *347*, 1138–1142.
7. Pollen, A.A., Nowakowski, T.J., Chen, J., Retallack, H., Sandoval-Espinosa, C., Nicholas, C.R., Shuga, J., Liu, S.J., Oldham, M.C., Diaz, A., et al. (2015). Molecular identity of human outer radial glia during cortical development. Cell *163*, 55–67.
8. Macosko, E.Z., Basu, A., Satija, R., Nemesh, J., Shekhar, K., Goldman, M., Tirosh, I., Bialas, A.R., Kamitaki, N., Martersteck, E.M., et al. (2015). Highly parallel genome-wide expression profiling of individual cells using nanoliter droplets. Cell *161*, 1202–1214.
9. Klein, A.M., Mazutis, L., Akartuna, I., Tallapragada, N., Veres, A., Li, V., Peshkin, L., Weitz, D.A., and Kirschner, M.W. (2015). Droplet barcoding for single-cell transcriptomics applied to embryonic stem cells. Cell *161*, 1187–1201.
10. Shekhar, K., Lapan, S.W., Whitney, I.E., Tran, N.M., Macosko, E.Z., Kowalczyk, M., Adiconis, X., Levin, J.Z., Nemesh, J., Goldman, M., et al. (2016). Comprehensive classification of retinal bipolar neurons by single-cell transcriptomics. Cell *166*, 1308–1323.
11. Bianco, I.H., and Wilson, S.W. (2009). The habenular nuclei: A conserved asymmetric relay station in the vertebrate brain. Philos. Trans. R. Soc. Lond. B Biol. Sci. *364*, 1005–1020.
12. Hikosaka, O. (2010). The habenula: From stress evasion to value-based decision-making. Nat. Rev. Neurosci. *11*, 503–513.
13. Namboodiri, V.M., Rodriguez-Romaguera, J., and Stuber, G.D. (2016). The habenula. Curr. Biol. *26*, R873–R877.
14. Proulx, C.D., Hikosaka, O., and Malinow, R. (2014). Reward processing by the lateral habenula in normal and depressive behaviors. Nat. Neurosci. *17*, 1146–1152.
15. Beretta, C.A., Dross, N., Guiterrez-Triana, J.A., Ryu, S., and Carl, M. (2012). Habenula circuit development: Past, present, and future. Front. Neurosci. Published online April 23, 2012. https://doi.org/10.3389/fnins.2012.00051.
16. Okamoto, H., and Aizawa, H. (2013). Fear and anxiety regulation by conserved affective circuits. Neuron *78*, 411–413.
17. Amo, R., Aizawa, H., Takahoko, M., Kobayashi, M., Takahashi, R., Aoki, T., and Okamoto, H. (2010). Identification of the zebrafish ventral habenula as a homolog of the mammalian lateral habenula. J. Neurosci. *30*, 1566–1574.
18. Agetsuma, M., Aizawa, H., Aoki, T., Nakayama, R., Takahoko, M., Goto, M., Sassa, T., Amo, R., Shiraki, T., Kawakami, K., et al. (2010). The habenula is crucial for experience-dependent modification of fear responses in zebrafish. Nat. Neurosci. *13*, 1354–1356.
19. Chou, M.Y., Amo, R., Kinoshita, M., Cherng, B.W., Shimazaki, H., Agetsuma, M., Shiraki, T., Aoki, T., Takahoko, M., Yamazaki, M., et al. (2016). Social conflict resolution regulated by two dorsal habenular subregions in zebrafish. Science *352*, 87–90.
20. Amo, R., Fredes, F., Kinoshita, M., Aoki, R., Aizawa, H., Agetsuma, M., Aoki, T., Shiraki, T., Kakinuma, H., Matsuda, M., et al. (2014). The habenulo-raphe serotonergic circuit encodes an aversive expectation value essential for adaptive active avoidance of danger. Neuron *84*, 1034–1048.
21. Okamoto, H. (2014). Neurobiology: Sensory lateralization in the fish brain. Curr. Biol. *24*, R285–R287.
22. Hong, E., Santhakumar, K., Akitake, C.A., Ahn, S.J., Thisse, C., Thisse, B., Wyart, C., Mangin, J.M., and Halpern, M.E. (2013). Cholinergic left-right asymmetry in the habenulo-interpeduncular pathway. Proc. Natl. Acad. Sci. USA *110*, 21171–21176.
23. deCarvalho, T.N., Subedi, A., Rock, J., Harfe, B.D., Thisse, C., Thisse, B., Halpern, M.E., and Hong, E. (2014). Neurotransmitter map of the asymmetric dorsal habenular nuclei of zebrafish. Genesis *52*, 636–655.
24. Kuan, Y.S., Yu, H.H., Moens, C.B., and Halpern, M.E. (2007). Neuropilin asymmetry mediates a left-right difference in habenular connectivity. Development *134*, 857–865.
25. Biran, J., Palevitch, O., Ben-Dor, S., and Levavi-Sivan, B. (2012). Neurokinin Bs and neurokinin B receptors in zebrafish-potential role in controlling fish reproduction. Proc. Natl. Acad. Sci. USA *109*, 10269–10274.
26. Dreosti, E., Vendrell Llopis, N., Carl, M., Yaksi, E., and Wilson, S.W. (2014). Left-right asymmetry is required for the habenulae to respond to both visual and olfactory stimuli. Curr. Biol. *24*, 440–445.
27. Jetti, S.K., Vendrell-Llopis, N., and Yaksi, E. (2014). Spontaneous activity governs olfactory representations in spatially organized habenular microcircuits. Curr. Biol. *24*, 434–439.
28. Kishimoto, N., Asakawa, K., Madelaine, R., Blader, P., Kawakami, K., and Sawamoto, K. (2013). Interhemispheric asymmetry of olfactory input-dependent neuronal specification in the adult brain. Nat. Neurosci. *16*, 884–888.
29. Zheng, G.X., Terry, J.M., Belgrader, P., Ryvkin, P., Bent, Z.W., Wilson, R., Ziraldo, S.B., Wheeler, T.D., McDermott, G.P., Zhu, J., et al. (2017). Massively parallel digital transcriptional profiling of single cells. Nat. Commun. *8*, 14049.
30. Picelli, S., Björklund, A.K., Faridani, O.R., Sagasser, S., Winberg, G., and Sandberg, R. (2013). Smart-seq2 for sensitive full-length transcriptome profiling in single cells. Nat. Methods *10*, 1096–1098.
31. Satija, R., Farrell, J.A., Gennert, D., Schier, A.F., and Regev, A. (2015). Spatial reconstruction of single-cell gene expression data. Nat. Biotechnol. *33*, 495–502.
32. Waltman, L., and Eck, N.J.V. (2013). A smart local moving algorithm for large-scale modularity-based community detection. Eur. Phys. J. B *86*, 471.
33. McDavid, A., Finak, G., Chattopadyay, P.K., Dominguez, M., Lamoreaux, L., Ma, S.S., Roederer, M., and Gottardo, R. (2013). Data exploration, quality control and testing in single-cell qPCR-based gene expression experiments. Bioinformatics *29*, 461–467.
34. Bayramli, X., Kocagöz, Y., Sakizli, U., and Fuss, S.H. (2017). Patterned arrangements of olfactory receptor gene expression in zebrafish are established by radial movement of specified olfactory sensory neurons. Sci. Rep. *7*, 5572.
35. Kitahashi, T., Ogawa, S., and Parhar, I.S. (2009). Cloning and expression of kiss2 in the zebrafish and medaka. Endocrinology *150*, 821–831.
36. Broms, J., Antolin-Fontes, B., Tingström, A., and Ibañez-Tallon, I. (2015). Conserved expression of the GPR151 receptor in habenular axonal projections of vertebrates. J. Comp. Neurol. *523*, 359–380.
37. Hirai, H., Pang, Z., Bao, D., Miyazaki, T., Li, L., Miura, E., Parris, J., Rong, Y., Watanabe, M., Yuzaki, M., and Morgan, J.I. (2005). Cbln1 is essential for synaptic integrity and plasticity in the cerebellum. Nat. Neurosci. *8*, 1534–1541.

38. Ngo, L., Haas, M., Qu, Z., Li, S.S., Zenker, J., Teng, K.S., Gunnersen, J.M., Breuss, M., Habgood, M., Keays, D.A., and Heng, J.I. (2014). TUBB5 and its disease-associated mutations influence the terminal differentiation and dendritic spine densities of cerebral cortical neurons. Hum. Mol. Genet. *23*, 5147–5158.

39. Jefferis, G.S., Potter, C.J., Chan, A.M., Marin, E.C., Rohlfing, T., Maurer, C.R., Jr., and Luo, L. (2007). Comprehensive maps of Drosophila higher olfactory centers: Spatially segregated fruit and pheromone representation. Cell *128*, 1187–1203.

40. Rohlfing, T., and Maurer, C.R., Jr. (2003). Nonrigid image registration in shared-memory multiprocessor environments with application to brains, breasts, and bees. IEEE Trans. Inf. Technol. Biomed. *7*, 16–25.

41. Randlett, O., Wee, C.L., Naumann, E.A., Nnaemeka, O., Schoppik, D., Fitzgerald, J.E., Portugues, R., Lacoste, A.M., Riegler, C., Engert, F., and Schier, A.F. (2015). Whole-brain activity mapping onto a zebrafish brain atlas. Nat. Methods *12*, 1039–1046.

42. Shalek, A.K., Satija, R., Adiconis, X., Gertner, R.S., Gaublomme, J.T., Raychowdhury, R., Schwartz, S., Yosef, N., Malboeuf, C., Lu, D., et al. (2013). Single-cell transcriptomics reveals bimodality in expression and splicing in immune cells. Nature *498*, 236–240.

43. Breiman, L. (2001). Random forests. Mach. Learn. *45*, 5–32.

44. Wong, M.K., Sze, K.H., Chen, T., Cho, C.K., Law, H.C., Chu, I.K., and Wong, A.O. (2013). Goldfish spexin: Solution structure and novel function as a satiety factor in feeding control. Am. J. Physiol. Endocrinol. Metab. *305*, E348–E366.

45. Appelbaum, L., Wang, G.X., Maro, G.S., Mori, R., Tovin, A., Marin, W., Yokogawa, T., Kawakami, K., Smith, S.J., Gothilf, Y., et al. (2009). Sleep-wake regulation and hypocretin-melatonin interaction in zebrafish. Proc. Natl. Acad. Sci. USA *106*, 21942–21947.

46. Habib, N., Li, Y., Heidenreich, M., Swiech, L., Avraham-Davidi, I., Trombetta, J.J., Hession, C., Zhang, F., and Regev, A. (2016). Div-Seq: Single-nucleus RNA-seq reveals dynamics of rare adult newborn neurons. Science *353*, 925–928.

47. Masland, R.H. (2001). The fundamental plan of the retina. Nat. Neurosci. *4*, 877–886.

48. Shimada, Y., Hirano, M., Nishimura, Y., and Tanaka, T. (2012). A high-throughput fluorescence-based assay system for appetite-regulating gene and drug screening. PLoS ONE *7*, e52549.

49. Dreosti, E., Lopes, G., Kampff, A.R., and Wilson, S.W. (2015). Development of social behavior in young zebrafish. Front. Neural Circuits *9*, 39.

50. Duboue, E.R., Hong, E., Eldred, K.C., and Halpern, M.E. (2017). Left habenular activity attenuates fear responses in larval zebrafish. Curr. Biol. *27*, 2154–2162.

51. Lénárd, L., László, K., Kertes, E., Ollmann, T., Péczely, L., Kovács, A., Kállai, V., Zagorácz, O., Gálosi, R., and Karádi, Z. (2018). Substance P and neurotensin in the limbic system: Their roles in reinforcement and memory consolidation. Neurosci. Biobehav. Rev. *85*, 1–20.

52. Normandeau, C.P., Ventura-Silva, A.P., Hawken, E.R., Angelis, S., Sjaarda, C., Liu, X., Pêgo, J.M., and Dumont, É.C. (2018). A key role for neurotensin in chronic-stress-induced anxiety-like behavior in rats. Neuropsychopharmacology *43*, 285–293.

53. Fore, S., Palumbo, F., Pelgrims, R., and Yaksi, E. (2017). Information processing in the vertebrate habenula. Semin. Cell Dev. Biol. Published online August 7, 2017. https://doi.org/10.1016/j.semcdb.2017.08.

54. Lovett-Barron, M., Andalman, A.S., Allen, W.E., Vesuna, S., Kauvar, I., Burns, V.M., and Deisseroth, K. (2017). Ancestral circuits for the coordinated modulation of brain state. Cell *171*, 1411–1423.

55. Campbell, J.N., Macosko, E.Z., Fenselau, H., Pers, T.H., Lyubetskaya, A., Tenen, D., Goldman, M., Verstegen, A.M., Resch, J.M., McCarroll, S.A., et al. (2017). A molecular census of arcuate hypothalamus and median eminence cell types. Nat. Neurosci. *20*, 484–496.

56. Gokce, O., Stanley, G.M., Treutlein, B., Neff, N.F., Camp, J.G., Malenka, R.C., Rothwell, P.E., Fuccillo, M.V., Südhof, T.C., and Quake, S.R. (2016). Cellular taxonomy of the mouse striatum as revealed by single-cell RNA-seq. Cell Rep. *16*, 1126–1137.

57. Zheng, G.X., Lau, B.T., Schnall-Levin, M., Jarosz, M., Bell, J.M., Hindson, C.M., Kyriazopoulou-Panagiotopoulou, S., Masquelier, D.A., Merrill, L., Terry, J.M., et al. (2016). Haplotyping germline and cancer genomes with high-throughput linked-read sequencing. Nat. Biotechnol. *34*, 303–311.

58. Ronneberger, O., Liu, K., Rath, M., Rueβ, D., Mueller, T., Skibbe, H., Drayer, B., Schmidt, T., Filippi, A., Nitschke, R., et al. (2012). ViBE-Z: A framework for 3D virtual colocalization analysis in zebrafish larval brains. Nat. Methods *9*, 735–742.

59. Marquart, G.D., Tabor, K.M., Horstick, E.J., Brown, M., and Burgess, H.A. (2016). High precision registration between zebrafish brain atlases using symmetric diffeomorphic normalization. Gigascience *6*, 1–15.

60. Langmead, B., and Salzberg, S.L. (2012). Fast gapped-read alignment with Bowtie 2. Nat. Methods *9*, 357–359.

61. Li, B., and Dewey, C.N. (2011). RSEM: Accurate transcript quantification from RNA-seq data with or without a reference genome. BMC Bioinformatics *12*, 323.

62. Brennecke, P., Anders, S., Kim, J.K., Kołodziejczyk, A.A., Zhang, X., Proserpio, V., Baying, B., Benes, V., Teichmann, S.A., Marioni, J.C., and Heisler, M.G. (2013). Accounting for technical noise in single-cell RNA-seq experiments. Nat. Methods *10*, 1093–1095.

63. Chung, N.C., and Storey, J.D. (2015). Statistical significance of variables driving systematic variation in high-dimensional data. Bioinformatics *31*, 545–554.

64. Hinton, G., and Maaten, L.d. (2008). Visualizing data using t-SNE. J. Mach. Learn. Res. *9*, 2579–2605.

65. Milligan, G.W., and Cooper, M.C. (1986). A study of the comparability of external criteria for hierarchical cluster analysis. Multivariate Behav. Res. *21*, 441–458.

66. Valente, A., Huang, K.H., Portugues, R., and Engert, F. (2012). Ontogeny of classical and operant learning behaviors in zebrafish. Learn. Mem. *19*, 170–177.

67. Dobin, A., Davis, C.A., Schlesinger, F., Drenkow, J., Zaleski, C., Jha, S., Batut, P., Chaisson, M., and Gingeras, T.R. (2013). STAR: ultrafast universal RNA-seq aligner. Bioinformatics *29*, 15–21.

68. Marquart, G.D. (2017). High-precision registration between zebrafish brain atlases using symmetric diffeomorphic normalization. GigaScience *6*, 1–15.

STAR★METHODS

KEY RESOURCES TABLE

REAGENT or RESOURCE	SOURCE	IDENTIFIER
Antibodies		
Anti-DIG POD	Roche	CAT#11 207 733 910
Anti-Flourescein-HRP	Roche	CAT#11 426 356 910
Anti-total-Erk	Cell Signaling	CAT#9102
Cy3 tyramide reagent	Perkin Elmer	CAT#NEL744991KT
Cy5 tyramide reagent	Perkin Elmer	CAT#NEL745001KT
Chemicals, Peptides, and Recombinant Proteins		
Earle's Balanced Salt Solution	Worthington	CAT#LS003126
Papain	Worthington	CAT#LS003126
Neurobasal	Thermo Fisher	CAT#21103049
B27	Thermo Fisher	CAT#A8806
BSA	NEB	CAT#B9000S
TCL Buffer	QIAGEN	CAT#1031576
1% 2-mercaptoethanol	Sigma	CAT#63689
Ovomucoid solution	Worthington	CAT#LS003087
Paraformaldehyde	Supplier Polysciences, Inc.	CAT#04018-1
Smart-seq2 reagents	[30]	N/A
Deposited Data		
Raw data files for RNA-sequencing	NCBI Gene Expression Omnibus	GSE105115
RNA-FISH Stacks	stackjoint.com	Search for Tags: "Pandey2017_WholeBrain," "Pandey2017_habenula"
Experimental Models: Organisms/Strains		
Tg(gng8-nfsB-CAAX-GFP)	Marnie Halpern [22]	N/A
Critical Commercial Assays		
NexteraXT	Illumina	CAT#FC-131-1024
RNAclean SPRI	Beckman Coulter Genomics	CAT#A63987
10X reagents	10X Genomics	Chromium Single Cell 3′v2 Reagent Kits
Software		
ImageJ		https://imagej.nih.gov/ij/index.html; RRID:SCR_003070
STAR (v2.4.0a)	[67]	https://github.com/alexdobin/STAR
Cellranger	10X chromium	https://support.10xgenomics.com/single-cell-gene-expression/software/pipelines/latest/what-is-cell-ranger
PCA, clustering, differential expression and	[31]	R library Seurat
t-distributed Stochastic Neighbor Embedding	[64]	https://lvdmaaten.github.io/tsne/
RSEM (v1.2.29)	[61]	http://deweylab.github.io/RSEM/
Bowtie2 (v2.2.7)	[60]	http://bowtie-bio.sourceforge.net/bowtie2/
RF Classification	[10] and this paper (See STAR Methods)	R package RF
CMTK	[40, 41]	N/A
ANTs	[68]	N/A
UMI based variable gene selection	This paper, see STAR Methods	N/A

CONTACT FOR REAGENT AND RESOURCE SHARING

Further information and requests for resources and reagents should be directed to and will be fulfilled by the Lead Contact, Alexander F. Schier (schier@fas.harvard.edu).

EXPERIMENTAL MODEL AND SUBJECT DETAILS

Zebrafish

Larvae and adult fish were maintained on 14 hr: 10 hr light: dark cycle at 28°C. All protocols and procedures involving zebrafish were approved by the Harvard University/Faculty of Arts & Sciences Standing Committee on the Use of Animals in Research and Teaching (IACUC; Protocol #25-08). Wild-type zebrafish from the TLAB strain were used. 10 days post fertilization (dpf) larval and ~1-year old adult male and female zebrafish were used across different experiments. Animals were anesthetized in 0.2% tricaine and rapidly euthanized by immersion in ice water for 5 min before dissection. RNA-seq experiments were performed with the transgenic lines: Tg(*gng8*:*nfsB*-CAAX-GFP) and Tg(*gng8*:GAL4XUAS:mCherry) in larval and adult stages. Tg(*gng8*: Gal4 X UAS: mCherry) was only used as a guide for dissection in adults.

METHOD DETAILS

Cell Isolation and RNA-Seq

Isolation of cells for SMART-seq2

10 dpf larval heads were dissected in Neurobasal (ThermoFisher Scientific 21103049) supplemented with 1x B-27 (ThermoFisher Scientific 17504044), and promptly dissociated using the Papain Dissociation Kit (LK003150) with following modifications. Larval heads were incubated in 20 units/mL papain for 25 min at 37°C. The cells were dissociated by gentle trituration 20 times and spun at 300xg for 5 min. The cells were resuspended in 1.1 mg/mL papain inhibitor in Earle's Balanced Salt Solution (EBSS). The resulting cell suspension was passed through 20 μm cell strainer and placed on ice. Two viability indicators (calcein blue, a live stain (ThermoFisher Scientific C1429) and ethidium homodimer, a dead cell stain (ThermoFisher Scientific E1169)) were added at a concentration of 0.01mg/mL. If the viability of cells was greater than 85% as measured by calcein blue staining, the cells were immediately sorted directly into a 96-well plate with 5μL of lysis buffer comprised of Buffer TCL (QIAGEN 1031576) plus 1% 2-mercaptoethanol (Sigma 63689). All samples were immediately frozen in dry ice and stored at −80°C until further processing.

SMART-seq2 library preparation

For preparation of SMART-seq2 libraries, the plates containing single-cell lysates were thawed on ice and purified with 2.2X RNAClean SPRI beads (Beckman Coulter Genomics) without elution. The beads were then air-dried and processed promptly for cDNA synthesis. SMART-seq2 was performed using the published protocol [30] with minor modifications [10]. We performed 22 cycles of PCR for cDNA amplification. The resulting cDNA was eluted in 10μL of TE buffer. We used 1.25 ng of cDNA from each cell and one fourth of the standard Illumina Nextera XT reaction volume in tagmentation, and final PCR amplification steps. We pooled 384 single-cell libraries from *gng8*-GFP line in each batch and sequenced 50x25 paired end reads using a single kit on the Illumina NextSeq500 instrument.

Cell isolation and library preparation for Droplet scRNA-seq

10dpf larval heads from 25 *gng8*-GFP fish were dissected, and cells were dissociated as described previously. After reconstitution of cells with papain inhibitor, the cells were spun again at 300xg for 5 min and washed with 1X Phosphate Buffered Saline (PBS). Viability indicators were added and roughly 6000-8000 cells were immediately sorted into 20μL of PBS to a final concentration of cells 300 cells/μL. The sorting was performed with a MoFlo Astrios (Beckman Coulter) with highly reduced sort pressure at 20psi. This was found to be a critical step as higher sorting pressure led to high cell death post sorting. The resulting single cell suspension was promptly loaded on the 10X Chromium system [57]. The sorted cells were not kept on ice for longer than 10 min because the viability post cell sorting, as measured by trypan blue staining, was found to drop over time.

For experiments with adult animals, six adult habenulae were directly dissected out of the brain based on the expression of *gng8*-GFP marker. The resulting tissue was then dissociated in 1mL of 20 units/mL papain for 15 min at 37°C. The habenular cells were dissociated by trituration, spun at 300xg for 5 min and resuspended in 1mL 1.1mg/mL papain inhibitor solution. The resulting cells were then washed in 1x PBS + 200mg/mL Bovine Serum Albumin (BSA) (NEB, B9000S) once and filtered through a 20 μm cell strainer. The cells were then resuspended in 50μL PBS + 200μg/mL BSA and counted on a hemocytometer. Viability was assessed by using a trypan blue staining and cells were loaded onto the 10X Chromium system at a concentration of ~300 cells/μL after ensuring that the cell viability in the suspension was greater than 80%. 10X libraries were prepared as per the manufacturer's instructions [57].

Imaging Methods

Probe synthesis for RNA ISH

Fragments of the following genes were amplified using Phusion Hi-Fidelity polymerase (New England Biolabs, M0530L) with the primers listed in Table S3. The Polymerase Chain Reaction (PCR)-amplified fragments were then cloned into pSC-A plasmid using Strataclone PCR Cloning Kit (Agilent, 240205), and used to transform the Strataclone competent cells. The transformed cells were plated overnight on Luria-Bertani (LB) agar plates. Colonies were selected by colony-PCR, cultured, mini-prepped and sent for

sequencing. The resulting plasmids were then restricted with the appropriate restriction enzyme (Table S3), and purified using PCR-clean up kit (Omega Cycle Pure Kit). The linearized vector was then used as a template to synthesize digoxigenin- or fluorescein-labeled RNA probes using the RNA labeling kit (Roche). The transcription reactions were purified using Total RNA clean up kit (Omega, R6834), and the resulting RNA was quantified using Nanodrop and assessed on an agarose gel. The final product was then normalized to a concentration 50ng/μL in HM+ buffer (50% formamide, 5X Saline Sodium Citrate (SSC) buffer, 5 mgmL^{-1} torula RNA, 50 μgmL^{-1} heparin, 0.1% Tween 20) and stored at −20°C until further use.

Fluorescent ISH

Fluorescent RNA ISHs were performed as previously described [58]. Zebrafish larvae were grown until 10dpf and were fixed in 4% formaldehyde (Sigma-Aldrich) in PBS at 4°C overnight. Post fixation, the larvae were rinsed three times in PBST (PBS with 0.1% Tween 20), and subsequently dehydrated in increasing concentrations of methanol (10 min each 25% methanol: 75%PBST, 50% methanol: 50% PBST, 75% methanol: 25% PBST and two times 100% methanol). Dehydrated larvae were then stored at −20°C at least overnight. Larvae were rehydrated with decreasing concentrations of methanol (10 min each, 75% methanol: 25% PBST, 50% methanol: 50% PBST, 25% methanol: 75% PBST, four times for 10 min PBST). They were digested in Proteinase K (10 μg/mL) for 1 hr and immediately fixed in 4% formaldehyde to stop digestion (20 min). Larvae were then pre-hybridized in Hybridization Mix (HM)+ buffer (50% formamide, 5 × SSC buffer, 5 mg/mL torula RNA, 50 μg/mL heparin, 0.1% Tween 20) at 65°C for 2 hr. Hybridization reactions with the RNA probes were carried out in HM+ (with digoxigenin-labeled antisense probes for single ISHs and digoxigenin- or fluorescein-labeled antisense probes for double ISHs) overnight at 65°C. Probes were normalized to a concentration of 3.33ng/μL and denatured at 70°C for 10 min before hybridization. Sense probe controls were performed alongside the antisense probes.

The next day, larvae were washed several times at 65°C (20 min in hybridization mix, 20 min in 75% formamide: 25% 2xSSCT (2XSSC with 0.1% Tween20), 20 min in 50% formamide: 50% SSCT, 20 min in 25% formamide: 75% SSCT, twice for 20 min in 2x SSCT, thrice for 30 min in 0.2x SSCT. The larvae were then washed twice in TNT (100mM Tris-HCl, pH 7.5, 150mM NaCl, 0.5% Tween 20) at room temperature. The larvae were subsequently blocked in 1% Blocking Reagent in TNT (TNTB) for at least 1 hr and incubated with a peroxidase-conjugated anti-digoxigenin-POD antibody (1:400 dilution in TNTB) at 4°C overnight with gentle agitation (Anti-Digoxigenin-POD Fab Fragments, Roche 11 207 733 910).

The following morning, the antibody was removed and larvae washed in TNT (8 times for 15 min each). After the washes, the larvae were stained per the TSA kit instructions for 1 hr in darkness without agitation (Perkin Elmer TSA Plus Cyanine 3 System, NEL744001KT). The larvae were then washed in TNT three times, 5 min each. For single in situs, a subsequent immunostaining for anti-total-Erk (Cell Signaling, 9102) was performed to use as an anatomical reference and signal for brain registration across multiple fish.

For double in situs, after the first staining reaction, the first antibody was removed by treating the larvae in 1% hydrogen peroxide for 20 min without agitation. The larvae were then incubated overnight with anti-fluorescein-HRP antibody (Anti-Fluorescein- POD Fab Fragments, Roche 11 426 356 910), diluted in 1:400 in blocking buffer at 4C with gentle agitation.

The following morning, the antiserum was removed and discarded, and excess antibody was removed by rinsing the embryos 8x15 min in TNT buffer. They were then subsequently stained by incubating in 100μL of Cy3 tyramide reagent diluted in 1:25 in amplification diluent (Perkin Elmer TSA PLUS Cyanine 3 System, NEL744991KT) for 1 hr without agitation. The embryos were then washed in 8X15 min in PBST and subsequently stained with anti-total-erk antibody for anatomical reference.

Fluorescent RNA ISH in adult zebrafish

Adult fish brains were dissected in ice-cold PBS and fixed overnight in 4% paraformaldehyde (PFA). Fluorescent RNA ISH in adult dissected brains was performed with the same protocol as outlined above with the following changes. Brains were digested in Proteinase K (20ug/mL) for 35 min. Following probe hybridization, antibody incubation and tyramide signal amplification, the brains were mounted in 3% low-melt (LM) agarose and sliced into 50 micron sections using the vibratome. The resulting slices were stained with TOPRO3 (1:5000) or Sytox green (1:30,000) for nuclear staining and imaged using a Zeiss inverted Confocal microscope with a 20X air objective and a 63X oil dipping objective.

Imaging and Image Registration

The larvae were washed three in PBST, mounted in 2% LM agarose and imaged with an upright Confocal Zeiss LSM 880 with a water dipping 20x objective.

Whole Habenula Registration

Image registration across multiple habenulae was performed with CMTK (https://www.nitrc.org/projects/cmtk/) with command string (-T 32 -awr 010203 -X 52 -G 80 -R 3 -A '–accuracy 0.8' -W '–accuracy 1.6'). Template habenula was a 10dpf nacre (mitfaa −/−) larvae that underwent RNA-FISH and immunostaining with anti-total-erk. All RNA-FISH images were subsequently registered to the same reference using cmtk [39-41]. All registered images were compared to the original *in situ* images to screen out unnatural morphing artifacts. The best registered images were chosen manually and used for generating reference habenula (Movie S1)

Whole Brain Registrations

Whole brain registrations were performed in a similar manner by choosing a reference whole brain image from a larva that underwent RNA-FISH and immunostaining with anti-total-erk. However, subsequent registrations were performed using Advanced Normalization Tools

ANTs [59] with the following parameters:

antsRegistration -d 3–float 1 -o [fish1_,fish1_Warped.nii.gz]–interpolation WelchWindowedSinc–use-histogram-matching 0 -r [Ref1.nii,fish1- 01.nii.gz,1] -t rigid[0.1] -m MI[Ref1.nii,fish1-01.nii.gz,1,32,Regular,0.25] -c [200x200x200x0,1e-8,10]–shrink-factors 12x8x4x2–smoothing-sigmas 4x3x2x1vox -t Affine[0.1] -m MI[ref/terk-ref.nii,fish1-01.nii.gz,1,32,Regular,0.25] -c [200x200x200x0, 1e-8,10]–shrink-factors 12x8x4x2–smoothingsigmas 4x3x2x1vox -t SyN[0.1,6,0] -m CC[ref/terk-ref.nii,fish1-01.nii.gz,1,2] -c [200x 200x200x200x10,1e-7,10]–shrink-factors 12x8x4x2x1–smoothingsigmas 4x3x2x1x0vox

Due to the high computation time required for these analyses, registrations were parallelized using Slurm-based bash scripts.

Image visualization

A non-linear gamma filter (ImageJ (Math; Gamma = 0.3)) was applied to the total-Erk channel in some images presented in the main text to aid visualization of the FISH signal.

Computational Methods for Data Analysis

Alignment and quantification

For the 10X droplet data, raw sequencing data was converted to matrices of expression counts using the cellranger software provided by 10X genomics[1]. Briefly raw BCL files from the Illumina NextSeq or HiSeq were demultiplexed into paired-end, gzip-compressed FASTQ files for each channel using ''cellranger mkfastq.'' Both pairs of FASTQ files were then provided as input to ''cellranger count'' which partitioned the reads into their cell of origin based on the 16bp cell barcode on the left read. Reads were aligned to a zebrafish reference transcriptome (ENSEMBL Zv10, release 82 reference transcriptome), and transcript counts quantified for each annotated gene within every cell. Here, the 10-base pair unique molecular identifier (UMI) on the left read was used to collapse PCR duplicates, and accurately quantify the number of transcript molecules captured for each gene in every cell. Both cellranger mkfastq and cellranger count were run with default command line options. This resulted in an expression matrix (genes x cells) of UMI counts for each sample.

For SS2 data, raw reads were mapped to a zebrafish transcriptome index (Zv10 Ensembl build) using Bowtie 2 [60], and expression levels of each gene was quantified using RSEM [61]. We also mapped the reads to the Zv10 genome using Tophat2. We only used libraries with genome alignment rate > 90% and transcriptome alignment rate (exonic) > 30%. RSEM yielded an expression matrix (genes x samples) of inferred gene counts, which was converted to TPX (transcripts per 10^4) values and then log-transformed after the addition of 1, consistent with the normalization of the droplet data.

Filtering expression matrix and correcting for batch effects

Cells were first filtered to remove those that contain less than 500 genes detected and those in which > 6% of the transcript counts were derived from mitochondrial-encoded genes (a sign of cellular stress and apoptosis). Genes that were detected in less than 30 cells were also removed. Among the remaining cells, the median number of UMIs per cell was 2,279 and the median number of genes was 1,319 for larval data. The same for adult data was 1,614 UMI/cell and 709 genes/ cell, respectively (Figures S1C, S1D, S5A, and S5B).

We used a linear regression model to correct for batch effects in the gene expression matrix using the RegressOut function in the Seurat R package, and used the residual expression values for further analysis. The residual matrix was then scaled, centered and used for the selection of variable genes, PCA and clustering.

Finding variable genes

To select highly variable genes in the data, we use two methods. For UMI-based droplet data, we derived a null mathematical model based on physical principles to model the relationship between average counts and the coefficient of variation (CV) across all the genes based on a negative binomial distribution (see below). This null model accurately estimated the minimum CV as a function of the mean counts across the full range, such that the actual CV for every gene was larger than the value predicted by our model. We used this model to rank genes based on the ''excess CV'' (difference between observed and predicted) and identified 706 highly variable genes (Figure S1F). This model fit droplet data very well (Figures S1E and S1F).

However, this model greatly underestimated the CV as a function of mean counts in SMART-seq2 data (Figures S4D and S4E), which was better captured by a similar, but more flexible mean-variance model developed earlier for SMART-Seq scRNA-seq data [62]. We speculate that this additional overdispersion in SMART-Seq data is due to amplification biases in the read counts in SMART-seq like protocols, which are not attenuated without UMIs. A similar analysis of droplet data with the raw read counts instead of UMIs supports the hypothesis that amplification biases are responsible for the overdispersion (Figure S4F). (see details in Section ''*Mean-CV model for transcript counts in UMI based data''* below).

We also used Seurat's data driven variable gene selection (FindVarGenes) method to identify highly variable genes in the SMART-seq2 data [31]. Briefly, the mean expression and dispersion (variance/mean) for each gene is computed across all single cells. The genes were then placed in 20 bins based on their mean expression. Within each bin, the dispersion of all genes was z-normalized to identify the genes that were highly variable within a similar average expression value. We identified 1,258 genes by this method. For our final analysis of the droplet dataset, we used a union of the variable genes selected with the two methods, which resulted in a total of 1436 variable genes. However, for SMART-seq2 data, which was generated without UMIs, we only used Seurat's dispersion method for variable gene selection.

Mean-CV model for transcript counts in UMI based data

The coefficient of variation (CV), defined as the ratio between the standard deviation (σ) of a variable and its mean (μ), is a natural measure of a gene's extent of variation. However, ranking genes based on decreasing expression CV leads to selection of genes

with low mean expression, particularly in count-based data. Hence, we sought to perform variable gene selection in droplet dataset by accounting for the mean-CV relationship. The simplest null model is that the transcript counts follow the Poisson distribution,

$$X_g \sim Poisson(\mu_g) \tag{1}$$

where X_g is the UMI counts for gene g in a cell, and μ_g is the sampling rate equal to the average count of gene g across all the cells. Since the variance of the Poisson distribution is equal to mean, this predicts a relationship: $CV_g = 1/\sqrt{\mu_g}$ (red dashed line, Figure S1F). The Poisson model, which is parameter-free, provides a tight lower bound of the CV for lowly expressed genes – i.e., the actual CV values for lowly expressed genes are equal to or higher than the Poisson CV. However, at high expression values we observed that the model significantly underestimates the minimum CV in the data. More specifically, the CV of genes in the data appears to plateau at high mean expression, whereas the Poisson model predicts a square root decrease.

What accounts for the over-dispersion in the data at high mean expression values compared to the Poisson model? According to the Poisson model, which treats genes independent of each other, the total number of transcript counts per cell (N_{tot}) is a sum of independent Poisson random variables, and therefore is a Poisson random variable itself. However, this is not supported by our data as the variance of N_{tot} is approximately 389 times its mean in the larval droplet data. This over-dispersion of total number of transcripts per cell for highly expressed genes could be caused by many factors. Some may be biological like cell size and cell state. However, many others may be technical factors such as variations in lysis and RT efficiency, number of captured oligonucleotides or extent of RNA degradation between droplets.

Based on this hypothesis, we made a simple modification to the Poisson model by positing that the sampling rate of a gene in a given cell depends on its relative library size η. We hypothesized that,

$$\eta = \frac{N_{tot,i}}{\mathbb{E}N_{tot,\,i}} \tag{2}$$

where $N_{tot,i}$ is the total number of molecules in cell i and $\mathbb{E}N_{tot,i}$ is its expectation across all cells. We note that $\mathbb{E}\eta = 1$. We found that a Gamma distribution with mean fixed at 1 provided an excellent fit for the empirical distribution of η in all of our droplet datasets (e.g., Figure S1E). Given the empirical distribution of η, we used the R package MASS to estimate the scale factor α for the Gamma distribution. This leads to a model where every gene is sampled from a Poisson distribution with its rate being a random variable following a Gamma distribution (our parameterization of η makes this a single parameter model).

Fortunately, this Gamma-Poisson mixture results in a closed form solution, wherein every gene follows a negative binomial distribution, $X_g \sim NB(r, p_g)$. Here, r and p represent the canonical parameters of the negative binomial distribution, the number of failures(r) and the success probability(p), which follow the relations,

$$r = \alpha,\ p = \frac{\mu_g}{\alpha + \mu_g} \tag{3}$$

Using standard properties of the negative binomial distribution, we compute the CV-mean relationship as,

$$CV_g^2 = \frac{1}{\mu_g} + \frac{1}{\alpha} \tag{4}$$

Figure S1F graphs this relationship (solid magenta line). As shown, for lowly expressed genes, we expect $1/\mu_g \gg 1/\alpha$, and the curve reduces to the Poisson regime. This suggests that for lowly expressed genes, the variation is dominated by the Poisson fluctuations. However, for highly expressed genes $\mu_g \gg \alpha$, the model reduces to $CV_g = 1/\sqrt{\alpha}$, explaining the saturation observed in the data. This suggests that for highly expressed genes the variation is dominated by various technical factors (contributing to library size differences) that result in more over-dispersion than predicted by the Poisson model. Importantly, through this simple modification, we were able to provide excellent estimates for the lower bound in CV across the full range of expression values. We ranked the genes based on their distance from this null curve in log-space, i.e., $\log(CV_{observed}/CV_{NB})$. We used the shape of the distribution of this quantity to estimate a cutoff value (0.3), above which genes were considered highly variable.

We note here that while Equation (4) models the baseline CV-mean relationships in transcript counts for UMI based data as a tight lower bound (Figure S1F), it significantly underestimates the CV-mean relationship observed in SMART-seq2 data (Figures S4D and S4E). Here, a related but more flexible model appears to perform better at capturing the mean-CV behavior [62],

$$CV_g^2 = \frac{\alpha_1}{\mu_g} + \frac{1}{\alpha_2} \tag{5}$$

This model [62], which we call the *Brennecke et al.* model, (Figure S4E, yellow line I $\alpha_1 = 205$, $\alpha_2 = 2.9$) better approximates the CV-mean relationship observed in SMART-seq2 data. This behavior is not peculiar to the SMART-Seq2 data presented in the paper. We reran the Poisson Gamma and the *Brennecke et al.* model on the read counts data from [5] and found that our model underestimates CV-mean relationship (Figure S4G). This overdispersion likely results from amplification bias in the non-UMI Smart-Seq2 data, because the Poisson Model accurately predicts mean-CV baseline in Drop-seq data of retinal bipolar neurons, produced by an alternative UMI-based protocol [10] (Figure S4H). We also verified this by analyzing read count data of larval droplet dataset prior to UMI collapse, which should "retain" amplification biases and found that the model performs worse with non-UMI based droplet dataset (Figure S4F).

Dimensionality reduction using PCA and Graph Clustering

Dimensionality reduction was performed using principal component analysis (PCA), and statistically significant PCs were identified using the Jackstraw function in Seurat [63]. 36 significant PCs were identified for larval and 30 significant PCs for identified for adult data. The scores of cells along these significant PCs were used to build a *k*-nearest neighbor graph, and partition the cells into transcriptionally distinct clusters using the smart local moving community detection algorithm [32] as implemented in the FindClusters function in Seurat. Subsequently, t-distributed stochastic neighbor embedding (tSNE) [64] was used to embed the cells based on statistically significant PCs, to visualize the graph clustering output on a 2D map. We note that the tSNE coordinates were computed independently of the cluster labels. All initial clusters were subjected to additional iterative clustering to discover additional heterogeneity within the initial clusters (Figure S1G). We found two additional droplet clusters (Hb05 and Hb12) and 1 additional SMART-Seq2 cluster by iterative clustering. We also verified that cells did not segregate based on their experimental batch id (Figures S4C and S5C) by observing the contribution of each experimental batch to every cluster in both adult and larval datasets. Downsampling experiments and assessment of cluster purity and entropy of the downsampled clusters were performed as described previously [10]. Adjusted Rand Index (ARI) for cluster consistency was calculated as described previously [65].

Marker genes discovery and quantification of their specificity and precision

Markers were nominated by performing a differential expression analysis between the cells in the cluster of interest and the rest of the cells in the dataset (Figure S1L). Markers' specificity and precision were quantified using a statistical test based on the area under the precision-recall curve (AUCPR). AUCPR is a quantitative measure of the balance between recall (the sensitivity of marker gene detection within the cluster of interest) and precision (accuracy of the quantitative levels of gene as a predictor of the correct cell type). Markers found by our analysis were either "digital" (expressed only in the marked cluster) with AUCPR values > 0.8, or analog (expressed at a higher level in the marked cluster, but also detectable in other clusters) with AUCPR values between 0.6-0.8. We compared the AUCPR values of marker and non-marker genes at a range of expression values and show that the marker genes have significantly higher AUCPR values compared to non-marker genes (Figure S2C). Markers with low AUCPR values belong to smaller clusters in which a small number of false positives in other clusters can significantly reduce the AUCPR value (Figure S2C, right panel).

Comparison of cluster signatures between droplet and SS2 datasets

Independent analysis of SMART-seq2 data revealed 10 clusters (Figure 4A), fewer than in the droplet data (Figure 1C). We hypothesized that the lower sample size might have masked subtle transcriptional differences between closely related sub-types, causing the corresponding clusters to merge. We reasoned that a supervised classifier trained on the signatures of the droplet dataset might be able to resolve these merged clusters in the SS2 dataset. Therefore, to evaluate the correspondence between the droplet and SS2 clusters rigorously, we trained a multi-class RF classifier on the droplet dataset. A RF is an ensemble learning method that consists of multiple decision trees, each of which are trained on a randomly defined set of features (genes) [43].

We composed a training set for the classifier by taking a sampling of cells from the 16 clusters from the droplet dataset. The number of training cells (N_k) from each cluster *k* was chosen such that N_k = min (500, $|cells_k|$*0.7), leading to the use of a maximum of 70% of the cells in each cluster for training. The remaining 30% of the cells in every cluster were used to test the classifier. In addition, the classifier was built on the most variable genes across both droplet and SS2 datasets. We trained the RF using 1,000 trees on the training set with the R package randomForest. This trained classifier was then used to assign a cluster label for the remaining 30% of the data. We assigned a class label to each cell, but only if a minimum of 15% of trees in the forest converged onto a decision (given that there are 16 classes, 6.25% vote would constitute a majority). Otherwise, the cells were labeled unassigned. Cells in the test set were accurately mapped to their correct classes by the trained classifier at a median rate of 95% for every cluster as reflected by the diagonal structure of the confusion matrix (Figure S4I).

This classifier was then used to predict the cluster labels of the cells in the SS2 dataset. It is important to note that the assignment is completely agnostic to the SS2 cluster label. After classifying each SS2 cell independently, we asked whether there was any correspondence between the SS2 clusters and the RF assignments to the droplet clusters. If greater than 70% of the cells of a single SS2 cluster mapped to single droplet clusters, that mapping was considered to be a 1:1 mapping. The Adjusted Rand Index (ARI, a measure of clustering consistency) between the RF assigned cluster labels and the SS2 labels was 0.45, significantly higher compared to the ARI between randomly permuted cluster labels and SS2 labels, which produced a maximum ARI value of 0.02 ($p < 0.001$).

Taken together, these results show that neuronal type-specific gene expression signatures that are important for cell type classification are robustly captured by sampling larger number of cells (with droplet) than a larger number of genes (with plate-based SS2).

Computation of entropy of cluster specific and extra SS2 genes

Compared to the droplet dataset, a host of extra genes in the SS2 dataset were expressed in a high proportion of cells but at lower expression level (Figures S4E and S4F). To understand the contribution of these "extra" genes in SS2, we identified all the genes that are expressed in moderate to high proportion of cells in the SS2 dataset but in a low proportion or not expressed in the droplet dataset (Figure S4L, red). We then tested if these genes could serve as good cluster-specific markers or enabled better cell type classification.

To assess the 'cluster-specificity' of these genes, we computed their Shannon entropy, H_g:

$$H_g = \sum_{1}^{n} p(x) \ln p(x)$$

Where p(x) is the probability of the finding gene g in cluster x. For a single gene g, H_g equals 0 if the gene is expressed in a single cluster, but increases in value if the gene is expressed across multiple clusters.

We compared the distribution of the Shannon entropy (low H_g, measure of cluster-specificity) for these ''extra'' SS2 genes to its distribution among marker genes, which as expected exhibited low values of H_g. A large majority of the ''extra'' genes detected in SS2 dataset had higher entropy values, suggesting that they are uninformative for cell type classification (Figure S4M).

Comparison of cluster signatures between larval and adult dataset

To systematically compare the larval and adult clusters, we used the expression of *gng8* to partition the adult clusters into ''high'' (average log (TPM + 1) > 2) and ''low'' (average log (TPM +1) < 2) *gng8*$^+$ cells. We used the ''high'' *gng8*$^+$ cells for further analysis (Figure S5F) as the *gng8*-GFP transgenic line was used to capture cells in the larval dataset (Figure 1B). We trained a multi-class RF classifier on our larval *gng8*-GFP droplet dataset as described above. We then used the RF model trained on the cluster signatures of the larval dataset to classify each adult cell into one of the larval habenular cluster labels, independent of the cell's adult cluster label. After classifying each adult cell independently, we asked whether there was any correspondence between the original clusters of the adult dataset and the RF-assigned clusters. This result was represented in the form of a confusion matrix as described in the SS2 cluster comparison section (Figure 5C). If greater than 70% of the cells of a single adult cluster mapped to a single larval cluster, that mapping was considered to be a 1:1 mapping. We verified that none of the adult cells mapped to larval cluster Hb16, which comprises olfactory placode cells that are labeled by the *gng8-GFP* transgenic line. These cells were not captured in the adult dataset as the adult dataset was generated by clean dissection of the habenula.

Functional experiments

Stimulation with electric shocks

For shock delivery, fish were placed in 85mm Petri dishes over which a 10 milli-second 7-V shock was delivered every 30 s for 30 min. Current was delivered using alligator clips as in a previously described apparatus [66]. Controls were placed beside the shocked fish and were also affixed with alligator clips but did not receive any shocks. Fish were then promptly fixed in 4% paraformaldehyde and subsequent RNA-FISH was performed for *cfos* expression.

These experiments were performed similarly in adults, except fish were kept in breeding cages during stimulation. After treatment with aversive stimuli, adult fish were rapidly killed by immersing in ice-cold water and their brains dissected immediately. Subsequent RNA-FISH was performed as described above to check for *cfos* expression in sub-populations within the habenula.

QUANTIFICATION AND STATISTICAL ANALYSIS

For experiments with larval habenula, cells were collected in three batches of SMART-seq2 data and one batch of 10X droplet data. For 10X experiment, 20 animals were pooled together in a single experiment. For SMART-seq2 experiments, batch 1 and batch 3 were composed of single animals whereas batch 2 was composed of 20 larval animals pooled together. For experiments with the adult habenula, cells were collected from age matched fish in two different experimental batches. Each batch was composed of 6 habenulae pooled together. For experiments involving RNA-FISH, each experiment was performed in batches of 20 fish. Approximately, 1000 larvae were imaged in total. For functional experiments in both larval and adult fish, experiments were performed in three independent batches. Within each batch, there were 20 treatment and 20 control animals for larva and 3 treatment and 3 control for adults.

All analysis related to RNA-seq was performed in R. Statistical methodologies and software used for performing various analysis in the paper are cited in appropriate STAR Methods section. Differential expression of genes across clusters in the 10X and SMART-Seq2 experiments was evaluated using bimodal and binomial test as described before[10].

Image registration analysis was performed in MATLAB and were parallelized using Slurm-based bash scripts.

DATA AND SOFTWARE AVAILABILITY

The accession number for the droplet and SMART-seq2 data reported in this paper is GEO: GSE105115.

ADDITIONAL RESOURCES

All whole brain and whole habenula Z stacks are available at: stackjoint.com. To explore the data, go to BasicViewer and search for Tag ''Pandey2017_Habenula'' for habenula stacks and ''Pandey2017_WholeBrain'' for whole brain stacks. Tags are also available in the dropdown menu.

[1]https://support.10xgenomics.com/single-cell-gene-expression/software/pipelines/latest/what-is-cell-ranger